Effect of copper and silver modification of NH_2-MIL-125(Ti) on the photoreduction of carbon dioxide to formic acid over this framework under visible-light irradiation

Mateusz A. Baluk [a],[*],[1], Aleksandra Pieczyńska [a],[2], Paweł Mazierski [a],[3], Malwina Kroczewska [b],[4], Kostiantyn Nikiforow [c],[5], Alicja Mikolajczyk [d],[e],[6], Joanna Dołżonek [f],[7], Justyna Łuczak [b],[8], Adriana Zaleska-Medynska [a],[*],[9]

[a] Department of Environmental Technology, Faculty of Chemistry, University of Gdańsk, Wita Stwosza 63, Gdansk 80-308, Poland
[b] Department of Process Engineering and Chemical Technology, Faculty of Chemistry, Gdańsk University of Technology, Gdańsk 80-233, Poland
[c] Institute of Physical Chemistry, Polish Academy of Science, Kasprzaka 44/52, Warsaw 01-224, Poland
[d] Laboratory of Environmental Chemoinformatics, Faculty of Chemistry, University of Gdańsk, Wita Stwosza 63, Gdansk 80-308, Poland
[e] QSAR Lab Sp. Z o. o, Trzy Lipy 3, Gdansk 80-172, Poland
[f] Department of Environmental Analysis, Faculty of Chemistry, University of Gdańsk, Wita Stwosza 63, Gdańsk 80-308, Poland

ARTICLE INFO

ABSTRACT

Cu and Ag enhance the photocatalytic activities of metal–organic frameworks (MOFs) toward CO_2 conversion because of their CO_2 adsorption capacities and effects on the lowest unoccupied molecular orbital (LUMO) overpotentials of MOFs. However, to date, targeted introduction of metals into MOFs to achieve visible (Vis)-light-active photocatalysts for CO_2 photoconversion has not been realized. Herein, a series of amine-functionalized Ti MOF (NH_2-MIL-125(Ti))-based photocatalysts were successfully synthesized using metalation, incorporation, and photodeposition, allowing Cu and Ag incorporation into NH_2-MIL-125(Ti) and attainment of ultraviolet- and Vis-light-active photocatalysts. Notably, the most active photocatalyst obtained by post-synthetic metalation of NH_2-MIL-125(Ti) by Cu^{2+} (MOF_met_0.5%Cu) demonstrated excellent performance in photoreducing CO_2 to HCOOH: a conversion rate of 30.1 umolg^{-1}h^{-1} and quantum yield of 1.18% at 380 nm. Photoconversion of CO_2 to HCOOH was further confirmed using $^{13}CO_2$. The novel approach proposed herein is a significant step toward clean energy production and environmental pollutant elimination.

1. Introduction

Environmental pollution and fossil fuel depletion are the main global issues that need to be addressed. Exploitation of fossil fuels has been linked to environmental degradation [1], ecosystem devastation, and the increase in the concentrations of CO_2 and other greenhouse gases in the atmosphere [2]. Therefore, developing new methods of energy and fuel production while simultaneously limiting environmental pollution is important. In this regard, photocatalytic reduction of CO_2 to useful fuels, such as methane, methanol, formic acid, and formaldehyde, using solar radiation exhibits considerable potential because it not only generates valuable chemical compounds using renewable source of energy (namely, solar energy), but also utilizes CO_2 as a substrate. However, new photocatalysts with high activities in the visible (Vis) light range and excellent selectivities are still in demand [3]. Recently, metal–organic frameworks (MOFs) have attracted significant interest as photocatalysts for CO_2 conversion. They are porous materials composed of secondary building units (SBUs) (that is, coordinated metal ions) joined by organic linkers [4]. MOFs are characterized by caged structures, large specific surface areas, and selectivities for chemical reactions. MOFs with open metal sites and specific groups (e.g.,–NH_2) in the linker demonstrate high CO_2 sorption capacities [4,5]. MOFs with photocatalytic properties exhibit outstanding sorption properties, and these MOFs include NH_2-MIL-125 (Ti) [6], NH_2-UiO-66 (Zr) [7], NTU-9 (Ti) [8], UiO-67 (Ce) [9], and PCN-222 (Zr) [10]. Their photocatalytic properties are ascribed to the presence of the -O-M-O- bonds, which result in the partially semiconducting natures of these MOFs [4,11].

For the practicality of MOFs in photocatalytic reactions such as hydrogen photogeneration and CO_2 photoconversion, MOFs should be characterized by appropriate highest occupied molecular orbital (HOMO)–lowest unoccupied molecular orbital (LUMO) potentials, which must be between the reduction potentials of the photocatalytic reaction [12]. The amine-functionalized Ti MOF - NH_2-MIL-125 (Ti) is one of the promising MOFs for the photoconversion of CO_2. Nevertheless, only few studies have been reported on the application of NH_2-MIL-125 (Ti) for CO_2 photoconversion (Table 1), where pristine

and modified NH_2-MIL-125 (Ti) have been applied for the photoconversion of CO_2 to HCOOH, methyl formate, methane, and CO. Different products were formed depending on the structure, modification, and form of MOF. Under Vis-light irradiation, Co/NH_2-MIL-125 (Ti) leads to HCOOH with a yield of 38.4 $\mu mol\ h^{-1}\ g_{cat}^{-1}$ [13]. NH_2-MIL-125 (Ti/Ni) results in CO, CH_4, and H_2 with yields of 5, 0.5, and 0.25 $\mu mol\ h^{-1}\ g_{cat}^{-1}$, respectively [14]. The rGO@NH_2-MIL-125 (Ti) composite generates methyl formate ($HCOOCH_3$) with a yield of 1116 $\mu mol\ h^{-1}\ g_{cat}^{-1}$ [15], whereas pristine NH_2-MIL-125 (Ti) produces CO and CH_4 with yields of 8.25 and 1.01 $\mu molh^{-1}g_{cat}^{-1}$, respectively [16]. Efforts are being made to increase the Vis-light activities of MOFs by modifying MOFs with various metals and compounds and manipulating the systems in which photoconversion occurs using different reaction media, photocatalyst concentrations, and processes. However, to date, the modification of NH_2-MIL-125 (Ti) with Cu and Ag to improve its CO_2 photoconversion activity has not been investigated. Ag or Cu modifications can potentially increase the separation of excited charges in photocatalysts [17–19] and enhance the photocatalytic activities under Vis-light irradiation [20] and photoreduction properties of photocatalysts [21]. Moreover, Cu is the only metal that exhibits high selectivity for the electrochemical reduction of CO_2 to hydrocarbons (including CH_4 and C_2H_4) [22–24]. Furthermore, theoretical calculation of the overpotential of CO_2 reduction to CH_4 indicates that the overpotential of CO_2 reduction to CH_4 over Cu is the closest to the volcano peak among those for all metal electrode materials [25]. Thus, the Cu ions/clusters included in the MOF structure demonstrate additional catalytic activities, enhancing the overall efficiency of the hybrid system. To the best of our knowledge, only Ao et al. [26] have reported a study on the Cu modification of NH_2-MIL-125 (Ti) (NH_2-MIL-125 (Ti/Cu)), and NH_2-MIL-125 (Ti/Cu) exhibited better properties in the photocatalytic degradation of organic pollutants (for instance, phenol and methyl blue). Several studies have described the impacts of modifying NH_2-MIL-125 (Ti) with Ag on the performances of NH_2-MIL-125 (Ti) in acetaminophen photodegradation [19] and water-splitting reactions [18]. Nevertheless, to the best of our knowledge, no information is available on the application of Cu- and/or Ag-modified NH_2-MIL-125 (Ti) for CO_2 photoconversion.

According to the theory of building units of MOFs reported by Prof. Yaghi, Cu can form SBUs or can become a part of the organic linker (metallolinker), whereas Ag can be incorporated into MOFs in the form of complexes only via modification of the linker [4]. Herein, we demonstrated that Cu-modified NH_2-MIL-125 (Ti) exhibited high performance in CO_2-to-HCOOH photoconversion under Vis-light irradiation (>420 nm). We speculated that different methods of NH_2-MIL-125 (Ti) modulation might affect the photoactivity of NH_2-MIL-125 (Ti); therefore, modifications of octahedral NH_2-MIL-125 (Ti) with Ag, Cu, and both Ag and Cu were realized by three methods: (*i*) metalation (post-synthetic addition of a metal to coordinating groups), (*ii*) photodeposition (post-synthetic formation of metal/metal oxide nanoparticles (NPs) on MOF surfaces), and (*iii*) incorporation (introduction of a second metal during MOF production and partial replacement of Ti). Effects of the type and amount of metal were systematically analyzed. The obtained materials demonstrated high porosities, high CO_2 sorption capacities, and high CO_2 photoconversion efficiencies under Vis-light irradiation. To prove that the detected HCOOH originated from CO_2 photoconversion and explain the mechanism of this reaction, photoconversion studies were performed using ^{13}C-labeled CO_2 followed by gas chromatography/mass spectrometry (GC/MS) and nuclear magnetic resonance (NMR) spectroscopy.

Table 1

Comparison of the most important currently available literature data on CO_2 photoconversion in the presence of NH_2-MIL-125 (Ti)-based photocatalysts and our results.

Sample name	Conditions for CO_2 conversion	Product and yield	Ref.
Co/NH_2-MIL-125 (Ti)	50 mg MOF in 60 mL AcN/TEOA (5/1, v/v), 300 W Xe lamp with UV-cutoff filter λ >420 nm	HCOOH38.4 $\mu molh^{-1}g_{cat}^{-1}$	[13]
NH_2-MIL-125 (Ti/Ni)	20 mg MOF on the glass fiber in 3 mL AcN and 1 mL TEOA, 30 kPa CO_2, 300 W Xe lamp, λ >350 nm	CO: 5 $\mu molh^{-1}g_{cat}^{-1}$ CH_4: 0,5 $\mu molh^{-1}g_{cat}^{-1}$ H_2: 0,25 $\mu molh^{-1}g_{cat}^{-1}$	[14]
rGO@NH_2-MIL-125 (Ti)	30 mg MOF in 30 mL MeOH, 300 W Hg lamp	$HCOOCH_3$: 1116 $\mu molh^{-1}g_{cat}^{-1}$	[15]
NH_2-MIL-125 (Ti)	10 mg MOF in 15 mL AcN, 1 mL H_2O, 3 mL TEOA, 300 W lamp Xe with UV-cutoff filter AM 1.5 G	CO: 8.25 $\mu molh^{-1}g_{cat}^{-1}$ CH_4: 1.01 $\mu molh^{-1}g_{cat}^{-1}$	[16]
PCN-222 (H_2)	2 mg MOF in 2 mL of 20 mM EG in water, 300 W lamp Xe with UV-cutoff filter λ >420 nm	HCOOH: 10.2 $\mu molh^{-1}g_{cat}^{-1}$	[47]
NH_2-UiO-66 (Zr)	50 mg MOF in 60 mL AcN/TEOA (5/1, v/v), 500 W Xe lamp with UV-cutoff filter λ >420 nm	HCOOH: 26.4 $\mu molh^{-1}g_{cat}^{-1}$	[48]
MOF_met_0.5% Cu	50 mg MOF in 20 mL AcN/TEOA (9/1, v/v), 1000 W Xe lamp with UV-cutoff filter λ >420 nm	HCOOH: 30.1 $\mu molh^{-1}g_{cat}^{-1}$ (AQY – 1.18%)	This work

2. Experimental

2.1. Materials

N,N-Dimethylformamide (DMF, p.a.), ethanol (EtOH, 99.8%), acetonitrile (AcN, >99.9%), and silver chloride (p.a.) were purchased

from POCh (Poland). Methanol (MeOH, p.a.) and acetic acid (AcA, 99.9%) were procured from Stanlab (Poland). 2-Aminoterephthalic acid (98%), titanium(IV) isopropoxide (TPOT, 98%), deuterated acetonitrile (AcN-d$_6$, 99.8%), deuterated dimethyl sulfoxide (DMSO-d$_6$, 99.8%), and C–^{13}C dioxide (99%) were purchased from Merck (Germany). Triethanolamine (TEOA) (99.8%) and copper nitrate hexahydrate (p.a.) were procured from Chempur (Poland).

2.2. Preparation of NH$_2$-MIL-125 (Ti)

NH$_2$-MIL-125 (Ti) (termed MOF hereinafter) was prepared via solvothermal synthesis [16]. 2-Aminoterephthalic acid (2.24 g) was dissolved in a mixture of 88 mL of mixtures of DMF, MeOH, and AcA in a 9/1/1 ratio (v/v/v). After dissolution 2.4 mL TPOT was added to the resulting mixture followed by incubation in an ultrasonic bath for 10 min. Thereafter, the acquired mixture was transferred to a Teflon cartridge followed by placement in an autoclave. The reaction was conducted at 150 ℃ for 24 h. To remove impurities from the MOF surface after synthesis, the first purification step was performed in which the powder was washed three times with DMF and MeOH and then washed with boiling DMF for 5 h [27]. Subsequently, it was washed three times with DMF and MeOH. Finally, the obtained material was activated for 3 days in MeOH followed by drying in a vacuum dryer at 200 ℃ for 5 h. The synthesis yield was 1.2 g.

2.3. Fabrication of modified NH$_2$-MIL-125 (Ti)

NH$_2$-MIL-125 (Ti) was modified with Cu, Ag, and a mixture of Cu and Ag by two post-synthetic methods (namely, metalation (met) and photodeposition (pho)) and one in-synthetic method (that is, incorporation (inc)). Detailed information about the acquired samples is provided in Table 2. All modified samples were reheated at 200 ℃ for 5 h under vacuum. Samples modified via inc before drying were purified in the same manner as that used for pristine MOF.

In metalation and photodeposition, pristine NH$_2$-MIL-125 (Ti) was prepared and then modified. In metalation, 200 mg MOF was added to 10 mL AcN in a scintillation vial. Cu^{2+} and Ag$^+$ precursor (Cu (NO$_3$)$_2$·6 H$_2$O and AgNO$_3$, respectively) solutions were added to the abovementioned MOF suspension to achieve a suspension with an appropriate weight ratio of metals and MOF. Theoretical amount of Cu in MOF was in the range of 0.25–1 wt%, whereas that of Ag was 0.5 wt%. Thereafter, the suspension was stirred for 24 h in the dark. Then, the resulting sample was centrifuged and washed three times with AcN and three times with MeOH followed by drying at 200 ℃ for 5 h in a vacuum dryer. The materials obtained using this method were denoted as MOF_met_x%metal (where x is the proportion of metal in MOF).

Table 2
Pristine and modified MOF samples.

Sample label	Type of synthesis method	Type of metal used as a modifier	Metal amount (wt%)
MOF	Solvothermal	-	-
MOF_**met**_0.5%Cu	Solvothermal synthesis	Cu	0.5%
MOF_**met**_0.5%Ag	followed by metalation	Ag	0.5%
MOF_**met**_0.5% Cu0.5%Ag		Ag	0.5%
		Cu	0.5%
MOF_**met**_0.25% Cu		Cu	0.25%
MOF_**met**_1.0%Cu		Cu	1.0%
MOF_**pho**_0.5%Cu	Solvothermal synthesis	Cu	0.5%
MOF_**pho**_0.5%Ag	followed by	Ag	0.5%
MOF_**pho**_0.5% Cu0.5%Ag	photodeposition	Ag and Cu	0.5%
MOF_**inc**_0.5%Cu	Solvothermal synthesis in	Cu	0.5%
MOF_**inc**_0.5%Ag	the presence of metal ions	Ag	0.5%
MOF_**inc**_0.5% Cu0.5%Ag		Ag and Cu	0.5%

In photodeposition, 200 mg MOF was suspended in 20 mL ethanol, and the resulting suspension was transferred to a quartz reactor. Subsequently, a solution of Cu^{2+} (Cu(NO$_3$)$_2$·6 H$_2$O) and/or Ag$^+$ (AgNO$_3$) was introduced into the suspension to acquire 0.5 wt%Cu- or/and 0.5 wt % Ag-modified MOF. Before deposition, O$_2$ was eliminated from the reactor by purging the reactor with N$_2$. To photodeposit Cu and Ag NPs, the resulting solution was irradiated with ultraviolet (UV)-Vis radiation (1000 W Xe lamp) for 1 h. The obtained material was centrifuged and washed three times with ethanol and methanol followed by drying at 200 ℃ for 5 h in a vacuum dryer. The samples acquired by this method were termed MOF_pho_x%metal (where x is the proportion of metal in MOF).

In the case of MOF modification by incorporation, a precursor solution of Cu^{2+} (Cu(NO$_3$)$_2$·6 H$_2$O) and/or Ag$^+$ (AgNO$_3$) was introduced into a mixture of DMF/MeOH/AcA during the solvothermal synthesis of MOF. The amount of Cu and/or Ag was equal to 0.5% by weight relative to that of MOF obtained under the same conditions. Production and purification conditions for the modified MOF were identical to those employed for pristine MOF. The samples acquired via this method were denoted as MOF_inc_x%metal (where x is the proportion of metal in MOF).

2.4. Characterizations of pristine and modified MOFs

Diffuse reflectance spectroscopy (DRS) was conducted using a UV-Vis spectrophotometer (SHIMADZU, UV-2600) in the wavelength range of 300–800 nm.

Photoluminescence (PL) spectra were recorded using an LS-50B luminescence spectrometer (Perkin Elmer) equipped with a Xe discharge lamp in the wavelength range of 300–700 nm at an excitation wavelength of 300 nm.

Fourier transform infrared (FTIR) spectra were obtained using an FTIR spectrometer (Nicolet iS5, Thermo Fisher) across a wavelength range of 400–4000 cm^{-1} using KBr as both a blank and matrix for the sample (10 wt% sample in KBr).

Morphological analyses were performed by scanning electron microscopy (SEM) using JEOL JSM-7610 F (JEOL) and transmission electron microscopy (TEM) coupled with energy-dispersive X-ray spectroscopy (EDS) using Titan G2 60–300 FEI (Field Electron and Ion Company).

Inductively coupled plasma (ICP) analysis of Cu and Ag was performed by EkotechLab (Poland) in accordance with PN EN ISO 11885:2009.

Brunauer–Emmett–Teller (BET) surface area, pore size and volume, and CO$_2$ sorption measurements were conducted using a Micro 200 sorption analyzer (3 P Instrument). CO$_2$ sorption test was performed under pressure in the range of up to p/p$_0$ (where p is the gas pressure and p$_0$ is the atmospheric pressure) - 0.97, which was approximately 1 bar in the range from −50–25 ℃, with a dosing rate of 30 mLg^{-1}. Pore size distribution was calculated using the Horvath-Kawazoe/Saito-Foley method, and heat of adsorption was evaluated using the 3 P-Instrument PAS program.

X-ray photoelectron spectroscopy (XPS) was conducted using a PHI 5000 VersaProbe spectrometer (Physical Electronics Incorporated) under the following conditions: monochromatic Al Kα radiation (hν = 1486.6 eV) and an X-ray source operating at 25 W, 15 kV, a spot size of 100 μm, a pass energy of 23.5 eV, and an energy step of 0.1 eV. The acquired XPS spectra were examined by CasaXPS using the set of the sensitivity factors native for the hardware. Shirley background and Gaussian–Lorentzian peak shapes were utilized for the deconvolution of all spectra.

Thermogravimetric analysis (TGA) was performed using Mettler Toledo TGA 2 (Mettler Toledo) in the temperature range of 50–800 ℃ at a heating rate of 10 ℃ min^{-1} under N$_2$ flow (50 mL min^{-1}).

X-ray diffraction (XRD) was conducted using a Rigaku MiniFlex 600 diffractometer (Rigaku Corporation) equipped with Cu Kα irradiation in

the 2θ range of 20–70.

2.5. Photocatalytic conversion of CO_2

Due to the difficulty in investigating the efficiency of CO_2 photoconversion caused by the production of fuels from the reaction of impurities existing on the photocatalyst rather than from CO_2 reduction [28], a series of processes were employed to purify the achieved materials. Before main photoconversion, MOFs were subjected a second purification step to remove impurities that could be converted to HCOOH or could interfere with the determination of HCOOH via ion chromatography (IC) by elution at the same retention time.

For this, various cleaning methods described in Supplementary Information (SI) (Text S1) were analyzed, and finally, photopurification was chosen as the best method for eliminating impurities from the photocatalysts. For each CO_2 photoconversion, 50 mg photocatalyst was suspended in a mixture of AcN and TEOA (9/1, v/v) with a total volume of 20 mL. Before each process, photopurification was performed for 2 h by continuously passing a N_2 stream via the system. After photopurification, the photocatalyst sample was centrifuged at 11,000 rpm followed by cleaning thrice with AcN. Thereafter, the purified photocatalyst was resuspended in AcN and TEOA (9/1, v/v) followed by transfer to a reactor with a quartz window and sealing with a rubber septum. Then, the electrolyte containing the photocatalyst was saturated with CO_2 by passing CO_2 gas via the reactor for 30 min at a flow rate of 0.4 Lmin^{-1}. Subsequently, the reactor was positioned near the radiation source (a 1000 W Xe lamp, Oriel) with a GG420 cut-off filter (λ > 420 nm). Samples (1 mL) were obtained at 1-h intervals during 4 h of illumination. Additionally, photoprocesses were conducted using the same conditions (namely, under UV-Vis and Vis-light irradiations) under a N_2 atmosphere and after CO_2 saturation in the dark. Liquid products (such as HCOOH) were examined by IC. Furthermore, the gas phase was analyzed to investigate the generation of other photoconversion products (including H_2, CO, and CH_3OH). The corresponding methodology is explained in SI (Text S2).

For MOF_met_0.5%Cu, a photocatalytic stability test was performed for over three cycles. After each cycle, the material was centrifuged followed by cleaning three times with AcN and drying at 60 °C. Additionally, for the analysis of the liquid sample after CO_2 photoconversion, the sample was analyzed as a mixture of 150 mgr KBr with 15 μL of the test sample (a mixture of 150 mgr KBr and 15 μL of AcN/TEOA mixture, 9/1, v/v, was used as a blank) using FTIR spectrometer (Nicolet iS5, Thermo Fisher).

2.6. Action spectrum analysis

Action spectrum measurements were conducted for MOF_met_0.5% Cu using the previously photopurified MOF_met_0.5%Cu (5 g) in a 2 mL solution of AcN/TEOA (9/1, v/v) saturated with CO_2. The reaction mixture was irradiated at monochromatic wavelengths (380, 400, 420, 440, 460, 480, and 500 nm) for 6 h. Light intensity was measured using an optical power meter (ILT2400, International Light Technologies). During the experiments, the reactor was maintained at 18 C, and the reaction mixture was continuously stirred. Liquid samples were examined by IC to determine the HCOOH concentration. Apparent quantum efficiency (AQE) as a function of wavelength was calculated based on the ratio of the rate of electron consumption to the flux of incident photons by speculating that two photons were required according to reaction stoichiometry [29,30]. AQE (%) was evaluated as follows:

$$AQE = \frac{N \times r}{P \Big/ \frac{hc}{\lambda}} \times 100\%$$

where N is the number of electrons needed to reduce CO_2 to HCOOH, r represents the rate of production of HCOOH molecules (mol s^{-1}), P is the

irradiation intensity (m W), h is the Planck constant (6.6261 × 10^{-34} J s), c denotes the speed of light in vacuum (2.998 × 10^8 m s^{-1}), and λ is the wavelength of light (m).

2.7. Photoconversion study with $^{13}CO_2$

To confirm the formation of HCOOH via CO_2 photoconversion, a study with isotopically labeled $^{13}CO_2$ was performed using MOF_-met_0.5%Cu (12.5 mg) in 5 mL AcN-d$_6$ under Vis-light irradiation (λ > 420 nm) for 10 h. The generated HCOOH was analyzed using ^{13}C NMR spectroscopy and GC/MS. ^{13}C NMR spectroscopy was conducted using a Bruker AVANCE III 700 MHz spectrometer, and undiluted liquid samples after photoconversion were directly investigated by NMR spectroscopy. To analyze HCOOH by GC/MS, derivatization was performed. For this, 1 mL liquid product was added to a glass vial (20 mL) containing 1 mL water with 0.1 mL concentrated H_2SO_4. Then, 1 mL ethanol was immediately introduced into the resulting mixture before analysis followed by heating at 80 °C under continuous stirring for 10 min. The derivatized product ethyl formate was examined by headspace GC/MS (GC-2010 Plus and GCMS-QP2010 SE Gas Chromatograph Mass Spectrometer, Shimadzu) using a SH-Stabliwax column; He was used as the carrier gas (injection volume: 200 μL, column temperature: 30 °C, purge flow: 3.0 mL min^{-1}, ion source temperature: 200 °C, and mass detection range: m/z 2–200). The entire mass spectrum and fragment ions at m/z of 74 and 75 (ethyl formate and ethyl [^{13}C] formate) were analyzed. In all analyses, the photoconversion products of normal CO_2 and standard solutions of HCOOH were investigated for comparison.

Additionally, ^{1}H NMR spectroscopy was conducted by a Bruker AVANCE III 700 MHz spectrometer. For this, liquid samples (10 μL) after photoconversion were added to a specific glass tube for NMR spectroscopy followed by the introduction of 0.5 mL DMSO-d$_6$.

2.8. Chemoinformatic analysis

In this study, principal component (PC) analysis (PCA) and experimental results were utilized to categorize a set of Cu and Ag MOFs according to their structural similarities. Subsequently, PCA was performed to determine potential correlations between the structures of the synthesized NH$_2$-MIL-125 (Ti)-based photocatalysts and their efficiencies in the photoreduction of CO_2.

PCA is a statistical technique commonly employed to simplify data by compression. This involves creating a new set of unrelated vectors from the initial dataset and examining the similarities between the investigated objects. In PCA, fresh variables, known as PCs, are formed as linear combinations of the original variables. The first PC accounts for the most significant portion of the variance in the original data matrix, whereas subsequent PCs explain the remaining unexplained variance. Essentially, each object in the original matrix is represented by a set of PCs rather than by original variables. With an increase in the number of PCs, the percentage of total variance explained decreases. Consequently, the number of PCs is typically substantially lower than that of the original variables because the total variance of the data is condensed into the initial PCs. Moreover, all PCs are orthogonal; that is, they are uncorrelated with each other, which is valuable during the analysis of potential similarities between objects. Thus, the information derived from an experimental study on the structures of chemicals was translated into numerical variables (so-called descriptors). Then, structural representations defined by the descriptors of the Cu and Ag MOFs were demonstrated in a two-dimensional (2D) space described by the first and second PC, as indicated by a score plot. To attribute physical meaning to each PC, we adhered to Malinowski's rule, considering only the contributions of descriptors with normalized loadings higher than 0.7 as significant.

Additionally, 2D hierarchical clustering analysis (HCA) unsupervised machine learning based on connecting similarities between objects in

the space of physicochemical characteristics mapped on the descriptor values and Euclidean distances was established.

3. Results and discussion

3.1. Morphologies of pristine and modified MOFs

Surface morphologies of the acquired materials were carefully examined. The obtained MOF particles exhibit octahedral shapes with sizes of 480 ± 153 nm. SEM images (Fig. S1a) reveal that the as-received pristine MOF comprises several impurities (e.g., reagent residues). Therefore, its purification included boiling in DMF at $155\,°C$ for 5 h [27] and activation in MeOH for 3 days (Fig. S1b). Then, the material was heated in a vacuum dryer at 200 C for 5 h (Fig. S1c) to evaporate residual solvents. Figures S1d and e show the SEM images of the samples after cleaning in EtOH and AcN/TEOA; nevertheless, these methods were not ultimately selected.

Fig. 1 depicts the SEM images of the purified MOF samples. Pristine MOF (Fig. 1a and S2) and all materials attained by post-synthetic methods (namely, met and pho) demonstrate octahedral structures with sizes in the range of 480 ± 153 nm. Ag and/or Cu modification of MOF by metalation induced small surface defects in the material (Fig. 1b and S2), and no metal NPs were observed. In the cases of MOF_pho_0.5% Ag (Fig. 1e and S2) and MOF_pho_0.5%Cu0.5%Ag (Fig. 1f and S2), spherical Ag NPs were generated on the MOF surfaces (Fig. 1), whereas NPs of copper oxides were detected in the cases of MOF_pho_0.5%Cu (Fig. 1c and S2) and MOF_pho_0.5%Cu0.5%Ag (Fig. 1f and S2). Sizes of the MOFs modified by incorporation were bigger than that of pristine MOF: 694 ± 174, 554 ± 116, and 637 ± 276 nm for MOF_inc_0.5%Cu (Fig. 1d and S2), MOF_inc_0.5%Ag, and MOF_inc_0.5%Cu0.5%Ag, respectively.

3.2. Investigations of crystal structures, surface compositions, and optical properties via XRD, FTIR, ICP, DRS, and XPS

XRD patterns of the pristine and modified MOFs in the 2θ range of $2–40°$ are shown in Fig. 2 and S3. All materials exhibit high crystallinities with similar diffraction peaks at $2\theta = 6.6$, 9.4, 9.6, 11.5, 13.4, 14.8, 15.2, 16.5, 17.8, 18.8, 19.4, 20.5, 21.6, 22.4, 23.3, 24.2, 24.8, 26.1, 27.9, 29.5, 32.4, 33.8, and $34.2°$, typical signals for pristine MOF [6,11, 26]. Peaks related to Ag NPs and Cu and Ag oxides were not noticed for all modified MOFs. The absence of peaks of these compounds is associated with their low concentrations in the fabricated materials [11].

FTIR spectra of the pristine and modified MOFs in the range of $500–4000$ cm^{-1} are depicted in Fig. S4. The spectrum of pristine MOF (black line) reveals distinct peaks characteristic of the MOF structure: (1) typical vibrational bands in the $1400–1670$ cm^{-1} region associated with the amine group of 2-aminoterephthalic acid in the coordinated Ti structure [31], (2) signals at $450–770$ cm^{-1} corresponding to Ti-O vibrations [31], and (3) signals at $2930–3620$ cm^{-1} attributed to the NH$_2$ group [31]. FTIR spectra of the samples modified with Ag demonstrate characteristic signals of Ag-N bonds at 679 cm^{-1} (pink arrow) [32] and Ag-O at 506 cm^{-1} (blue arrow) [33]. In the spectrum of MOF modified with Cu, signals at 956 and 1054 cm^{-1} corresponding to the Cu-N bond (red arrow) are observed [34].

ICP results are presented in Table S1. Predicted and actual amounts of metals in the post-synthetically modified Ag and Cu samples (that is, met and pho samples) are slightly different. The amount of Cu in MOF_inc_0.5%Cu is 0.15 wt%, whereas the amount of Ag in MOF_inc_0.5%Ag is 0.13 wt%. Lowest amounts of these metals are noticed for MOF_inc_0.5%Cu0.5%Ag, in which the contents of Ag and Cu are 0.07 and 0.04 wt%, respectively. The amounts of metals in the modified samples obtained by Ag and Cu inc are significantly lower than the estimated amounts. Because of MOF synthesis, the incorporations of Ag$^+$ and Cu^{2+} into the MOF structure were supposed to be unsuccessful, forming a small amount of mixed SBUs together with Ti^{4+}.

Figure S8a shows the corresponding solid-state UV-Vis absorbance spectra acquired via DRS for all the prepared samples in the range of 300–800 nm. The spectra of both pristine and modified MOFs exhibit a maximum absorption peak at 386 nm. Using the Kubelka-Munk transformation, the energy gap for pristine MOF was determined to be 2.76 eV, which is in agreement with that reported in the literature (Fig. S8b) [11,16]. Each modification of MOF with Ag, Cu, and Ag and Cu decreased the irradiation absorbance in the UV range and increased the irradiation absorbance in the Vis range, which was consistent with the findings reported in the literature [26]. Furthermore, the signal at 700 nm observed in the spectrum of MOF_inc_0.5%Ag may be related to the presence of plasmons arising from Ag NPs on the MOF surface [35].

Owing to the semiconducting properties of MOFs, the PL properties of the fabricated materials were investigated. Based on the PL spectra, the recombination rate and types of electron transitions after excitation were compared. Recombination of excited electrons is slower if the PL maxima demonstrates low intensity [36]. Figure S9 depicts the PL spectra in the range of 300–700 nm ($\lambda_{ex} = 300$ nm) for the obtained MOFs. The red line represents the PL spectrum of pristine MOF, which is characterized by two strong emission peaks at 458 and 500 nm. During excitation by electromagnetic radiation, electrons from the HOMO level of the nitrogen atom (n, p) are excited to the LUMO level of the C-O bond (π^*), followed by a transition to coordinated Ti structures (Ti 3d).The emission is initiated by recombination of excited electrons present at the Ti3d level with the resulting holes present at the HOMO level of the nitrogen atom as shown in Figure S9b [37]. Modifications of MOFs with Cu, Ag, or Cu and Ag decrease the PL intensity, which is in agreement with previous studies, implying slower recombination of reactive electron–hole pairs [38,39]. The highest decrease was noticed when Ag was employed for MOF modification regardless of the method used. Slowest recombination of electron–hole pairs implied by the lowest PL intensity was observed for MOFs modified by photodeposition.

XPS was performed to evaluate the presence and chemical states of elements (Fig. S10 and Table S3). The main point of interest was the estimation of the chemical states and possible bonding of Cu and Ag depending on the kind of sample modification. Cu2p and Ag3d spectra were recorded for Cu and Ag, respectively. Standard survey spectrum for MOF_pho_0.5%Cu0.5%Ag is shown in Fig. S11.

In all the examined samples, the contents of Cu and Ag are substantially low (approximately 0.2–0.4 at%) and these contents are particularly low (below 0.1 at%) in case of the inc modification. XPS results and literature analysis revealed the way Cu^{2+} and Ag$^+$ were connected to MOF. In the cases of the samples modified by metalation, Cu2p3 peak is obtained at the binding energy (BE) of 933.1 eV, whereas that of Ag3d5 is acquired at a BE of 368.5 eV. These BEs are less typical for the oxidized compounds of Cu and Ag [40], and the metal ions probably coordinate with the amine groups of the linker 2-aminoterephthalic acid, affording MOF_met [41,42]. For the photodeposited samples, the position of the Cu2p3 peak (at a BE of approximately 932.8 eV) suggests that Cu forms copper (I) oxide [43] on the MOF surface [44,45]. However, the results for the Ag modification of MOF are mixed. The Ag3d5 peak is observed both above and below 368 eV BE, which indicates that aside from silver oxide [40], metallic Ag or bonding similar to that in the metalation samples may be present.

As mentioned earlier, in the case of incorporation modification, the Cu and Ag concentrations in the samples are low, complicating the evaluation of element bonding. Nevertheless, considering the positions of Cu2p3 (932.6 eV) and Ag3d5 (368.4 eV) peaks and literature data [26], we propose that metal ions are incorporated into the MOF crystal lattice (SBU). For MOF_inc_0.5%Ag, the signals are located above 368 eV, suggesting the existence of metallic Ag or organic complexes. XPS results and literature analysis indicated the possible mode of interaction of Cu^{2+} with MOFs (Fig. 3). In metalation, Cu and Ag presumably connect to the material via a coordination bond with the linker amino groups. In incorporation, Cu and Ag are incorporated into the structures of SBUs of MOFs, whereas when Ag is incorporated into SBUs
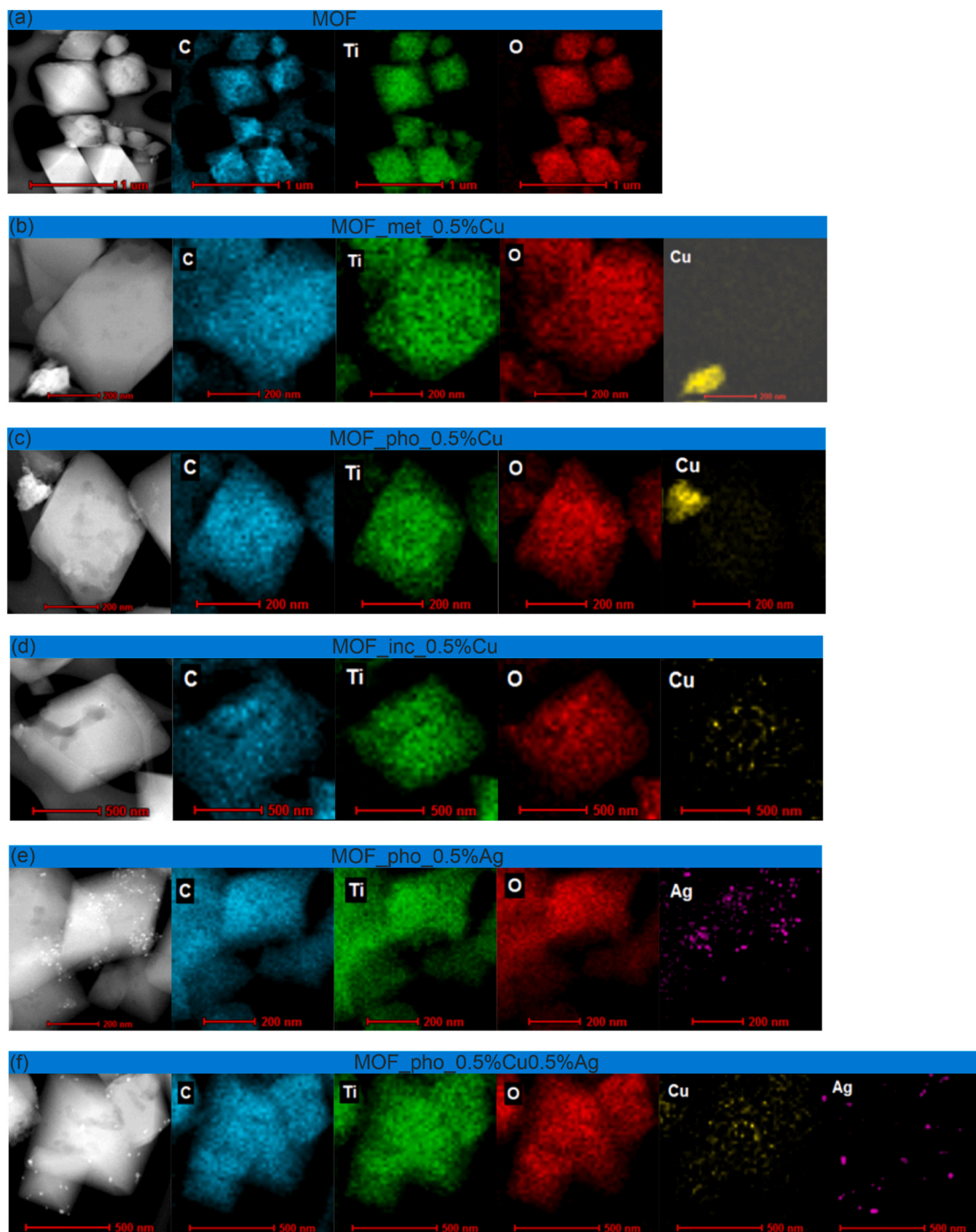
Fig. 1. STEM images with EDS mappings for (a) MOF (pristine NH$_2$-MIL-125 (Ti)), (b) MOF_met_0.5%Cu, (c) MOF_pho_0.5%Cu, (d) MOF_inc_0.5%Cu, (e) MOF_pho_0.5%Ag, and (f) MOF_pho_0.5%Cu0.5%Ag.
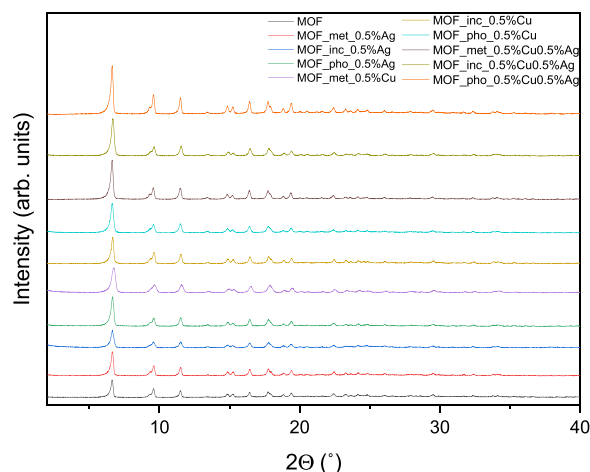
Fig. 2. X-ray diffraction (XRD) patterns of the MOF samples in the 2θ range of 2–40.

of MOFs, Ag^0 NPs are formed. In pho, copper(I) oxide or Ag_2O/Ag NPs are generated.

3.3. Sorption properties

Specific BET surface areas and CO_2 sorption capacities of pristine MOFs depend on the purification and activation methods (Table S2). MOF before the first step of purification exhibits a surface area of 868 m^2 g^{-1} and CO_2 sorption capacity of 1.02 mmol g^{-1}, which is similar to those reported in previous studies [11,16]. After purification of MOF in boiling DMF followed by three-day activation in MeOH and drying at 200 °C under vacuum, the surface area and CO_2 sorption capacity increased to 1376 m^2 g^{-1} and 6.16 mmol g^{-1}, respectively. Lower BET surface area and CO_2 sorption capacity are observed in the case of non-purified MOF because of the presence of post-synthesis contaminants including unreacted precursors, which can be noticed in the SEM images of the MOF samples (Fig. S1a). BET surface areas, CO_2 sorption capacities, and pore characteristics of pristine MOF and MOFs modified with Ag and/or Cu are provided in Table 3. Additionally, N_2 and CO_2 sorption isotherms are depicted in Fig. S5 and S6. For all samples, the adsorption–desorption of N_2 was examined, and the isotherm demonstrates a type I shape. BET surface areas and CO_2 sorption capacities of modified MOFs with 0.5 wt% metal were lower than those of pristine MOFs. The highest decrease in the BET surface area is observed for the Ag-modified samples, which is probably caused by the existence of a
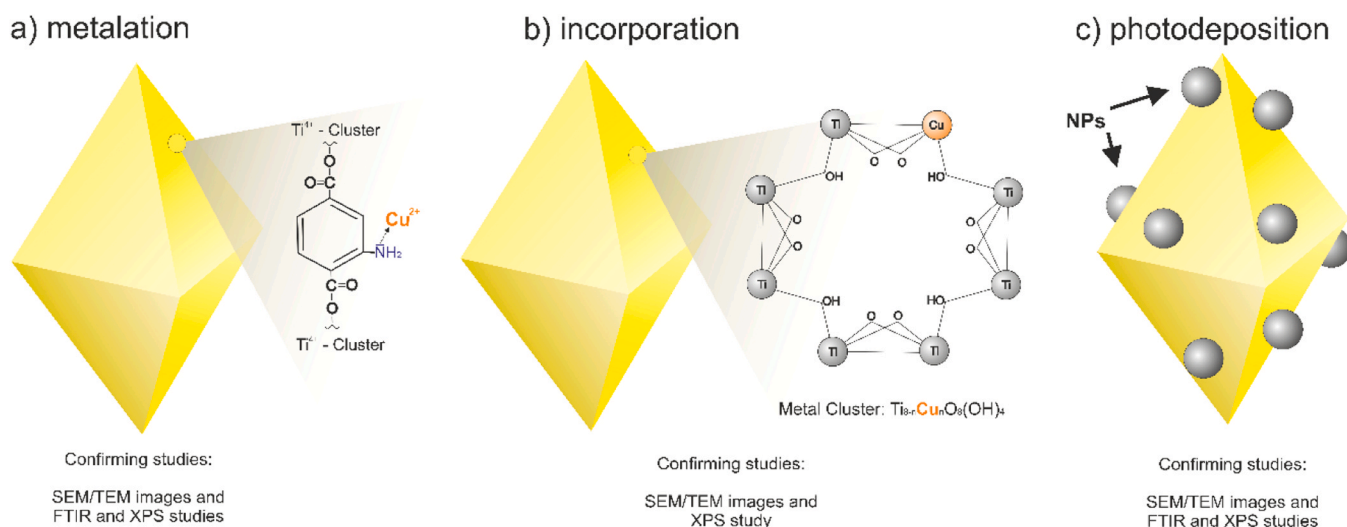

Fig. 3. Schematic models of Cu^{2+}-modified MOFs and the corresponding binding sites.

Table 3

CO_2 sorption capacities under ~1 bar (p/p₀: ~0.97), BET surface areas, and pore characteristics of pristine and modified MOFs.

Sample name	CO_2 sorption (mmol g^{-1})	BET Surface Area (m^2g^{-1})	Pore Volume at $p/p_0 = 0.99$ (cm^3g^{-1})	The most frequent pore diameter (nm)	Median pore diameter (nm)
MOF	6.16	1376	0.65	0.45	0.53
MOF_**met**_0.5%Cu	4.15	1323	0.66	0.47	0.53
MOF_**met**_0.25%Cu	4.20	1395	0.64	0.52	0.54
MOF_**met**_1.0%Cu	3.84	1402	0.76	0.39	0.43
MOF_**met**_0.5%Ag	4.08	924	0.57	0.46	0.52
MOF_**met**_0.5%Cu0.5% Ag	4.85	1096	0.52	0.43	0.47
MOF_**pho**_0.5%Cu	4.19	1346	0.68	0.36	0.43
MOF_**pho**_0.5%Ag	4.74	1218	0.60	0.46	0.53
MOF_**pho**_0.5%Cu0.5% Ag	4.34	933	0.62	0.49	0.55
MOF_**inc**_0.5%Cu	3.26	1160	0.54	0.42	0.44
MOF_**inc**_0.5%Ag	3.78	969	0.65	0.47	0.54
MOF_**inc**_0.5%Cu0.5% Ag	3.94	1000	0.66	0.47	0.54

large Ag atom (or Ag compounds) inside the structures or on the surfaces of MOFs. For Cu-modified MOFs, the BET surface areas were slightly lower than that of pristine MOF, which were 1323, 1346, and 1160 $m^2 g^{-1}$ for MOF_met_0.5%Cu, MOF_pho_0.5%Cu, and MOF_inc_0.5%Cu, respectively. Moreover, the CO_2 sorption capacities of the same samples were significantly lower than that of pristine MOF, which were 4.15, 4.19, and 3.26 mmol g^{-1} for MOF_met_0.5%Cu, MOF_pho_0.5%Cu, and MOF_inc_0.5%Cu, respectively. The considerably low sorption capacity and BET surface area of MOF_inc_0.5%Cu may be related to the structural changes induced by the presence of Cu. Furthermore, the CO_2 sorption capacities decreased with an increase in the amounts of Cu in MOFs modified by metalation. The CO_2 sorption capacities for MOFs comprising 0.25, 0.5, and 1.0 wt% Cu were similar (4.20, 4.15, and 3.84 mmol g^{-1}, respectively). The decrease in the CO_2 sorption capacity with an increase in the amounts of Cu in MOFs may be ascribed to the binding of Cu to the N atom of the amino group (Fig. 3), thus blocking its CO_2-binding properties. Comparison of the CO_2 sorption capacities of MOFs modified by different methods reveals that MOFs modulated by inc exhibit the lowest CO_2 sorption capacities. Pore volume and diameter of pristine MOF were 0.65 $cm^3 g^{-1}$ and 0.45 nm, respectively. No significant differences were noticed between the pore volumes and diameters of Ag- and Cu-modified samples. Heats of adsorption were determined for pristine MOF and MOFs modified with Ag and/or Cu based on the CO_2 adsorption–desorption isotherms at 223 and 298 K (Fig. S7b). Heat of adsorption decreased in the CO_2 dose range of 25–90 $cm^3 g^{-1}$ for all tested samples (except for MOF_inc_0.5% Cu0.5%Ag). Cu-modified MOF demonstrates the highest heat of adsorption regardless of the modification method. Heat of adsorption for MOF_met_0.5%Cu is 19.52 kJ mol^{-1} on average, whereas those for MOF_pho_0.5%Cu and MOF_inc_0.5%Cu are 16.93 and 10.94 kJ mol^{-1}, respectively. Temperature-dependent characterization of CO_2 sorption capacity for MOF_met_0.5%Cu (Fig. S7a) indicates that the CO_2 sorption capacity decreases from 12.8 to 4.15 mmol g^{-1} with an increase in temperature from 223 to 298 K.

3.4. Photocatalytic conversion of CO_2

3.4.1. MOF purification methods (initial step of photocatalytic conversion)

Preliminary studies of the photoconversion of CO_2 to HCOOH were conducted using pristine MOF as a photocatalyst and a solution of AcN with 10% TEOA as an electrolyte. Suspension of MOF (acquired after the first purification step) in the electrolyte solution was purged with CO_2 for 30 min, and then, 4-h photoconversion under UV-Vis irradiation was initiated. To verify that HCOOH was produced from CO_2, a blank test was performed by purging the MOF solution with N_2 instead of CO_2. The results shown in Fig. S12 reveal negligible difference between the amounts of HCOOH generated after 4 h of irradiation under N_2 (279 μmol g^{-1}) and CO_2 (289 μmol g^{-1}) atmospheres. Signals corresponding to HCOOH detected in the IC chromatograms in the case of N_2 may have originated from the unreacted precursors adsorbed on the pores of MOF and formed in the results of DMF decomposition during synthesis or first step of purification [4]. Therefore, herein, several MOF purification methods were analyzed, and after each method, the generation of HCOOH under a N_2 atmosphere via a 2-h process under UV-Vis irradiation was examined (Fig. S13). Although 24-h purification of MOF by shaking it in AcN, AcN/TEOA, or EtOH reduced HCOOH production, the amount of generated HCOOH was still in the range of 139–174 μmol g^{-1}. The best results were obtained when MOF was purified in the electrolyte (AcN with 10% TEOA) for 2 h under UV-Vis irradiation (photopurification), which reduced the amount of produced HCOOH to below 10 μmol g^{-1}. Consequently, before each photocatalytic process, MOF was subjected to photopurification (that is, the second step of purification and initial step of photocatalytic conversion).

3.4.2. CO_2 photoconversion by pristine and modified MOFs

CO_2 photoconversion efficiencies of pristine MOF (after

photopurification) under a CO_2 atmosphere after 4 h of reaction were 85.2 and 53.6 μmol g^{-1} under UV-Vis and Vis-light irradiations, respectively (Fig. S14). In contrast, under a N_2 atmosphere, generating formic acid were 5.6 and 2.7 μmol g^{-1}. For reference, the electrolyte solution under N_2 and CO_2 atmospheres was separately irradiated with UV-Vis, and in both cases, no HCOOH was generated. Catalytic formation of HCOOH in the absence of light was also not detected. Additionally, the production of gaseous products (H_2, CO, and CH_4) during photoconversion was investigated, and no significant amounts of these products were observed.

Fig. 5 depicts the kinetics of HCOOH generation under Vis-light irradiation using MOFs modified with Cu, Ag, and both metals via the three methods. Highest photoconversion efficiency (120.4 μmol g^{-1} in 4 h) was acquired for MOF_met_0.5%Cu. Lower photoconversion efficiencies (105.0 and 71.8 μmol g^{-1}) were obtained for MOF_pho_0.5%Cu and MOF_inc_0.5%Cu, respectively. HCOOH generation efficiencies were slightly higher for MOFs modified with Ag by metalation and photodeposition. However, the HCOOH generation efficiency of MOF_inc_0.5%Ag was lower than that of pristine MOF. Moreover, the HCOOH generation efficiency of MOF_pho_0.5%Cu0.5%Ag was lower (35.6 μmol g^{-1}) than that of pristine MOF. The low HCOOH production efficiency can potentially be attributed to the formation of Ag NPs on the MOF surface. This occurrence arises from the low Fermi levels of Ag NPs, leading to the confinement of accumulated electrons in the LUMO band of MOF or Cu_2O. Consequently, the recombination of electrons and holes is effectively suppressed, as evidenced by the PL spectra shown in Fig. S13 [46]. Nevertheless, this process simultaneously impedes the reduction of CO_2 because the electrons do not rapidly reduce CO_2 and are instead accumulated in Ag NPs.

CO_2 photoreduction efficiency of MOF_met_0.5%Cu is similar to that of Co/NH_2-MIL-125 (Ti), which was obtained by Fu et al. [13] and examined under similar photochemical conditions (38.4 μmol h^{-1} g_{cat}^{-1} yield). Additional literature reports the use of MOF or modified MOF under different photoreduction conditions (radiation- and solution-based conditions). Chen et al. [14] synthesized NH_2-MIL-125 (Ti/Ni), which resulted in a total efficiency of 5.75 μmol h^{-1} g_{cat}^{-1} (CO, CH_4, and H_2) when exposed to radiation with $\lambda > 350$ nm; furthermore, Cheng et al. [16] obtained a pristine MOF that generated a total of 9.26 μmol h^{-1} g_{cat}^{-1} products (CO and CH_4) when exposed to simulated sunlight using filter AM 1.5 G. In addition, the resulting material shows better performance photoreduction of CO_2 compared to other MOFs tested under similar exposure conditions, for example with PCN-222 (H_2) [47] and NH_2-UiO-66[48]. Potentially, some MOFs encapsulated in a conductive membrane or deposited on a conductive layer could serve as a catalyst for photoelectroreduction [49,50] or electroreduction reactions [51–54] of CO_2 to acids and alcohols as previous studies show. However, although the use of MOFs in photoeletroreduction or electroreduction processes can boost the efficiency of product generation, these technologies require application of voltage, and therefore more energy consuming and expensive.

For MOF modification, selecting an appropriate amount of modifier is important. Therefore, the effect of the Cu amount in the range of 0.25–1 wt% used for MOF modification by metalation on the HCOOH generation efficiency was analyzed (Fig. S15). For MOF_met_0.25%Cu and MOF_met_1.0%Cu, the efficiencies of CO_2 photoconversion to HCOOH in 4 h are 41.6 and 81.2 μmol g^{-1}, respectively, which are considerably lower than that of MOF_met_0.5%Cu. These efficiencies are significantly lower than that of NH_2-MIL-125 (Ti) metallized with Co (2% wt.), which exhibits the highest HCOOH production efficiency [16]. In contrast, Ao et al. [26] modified NH_2-MIL-125 (Ti) with Cu via an incorporation method. The incorporation of 1.5 wt% Cu into the MOF material resulted in the highest efficiency for the photodegradation of methyl blue and phenol under Vis-light irradiation.

Note that the HCOOH generation efficiency is related to the heat of CO_2 adsorption by pristine and metallized MOFs. The highest heat of adsorption is detected for MOF_met_0.5%Cu (19.5 kJ mol^{-1}), which
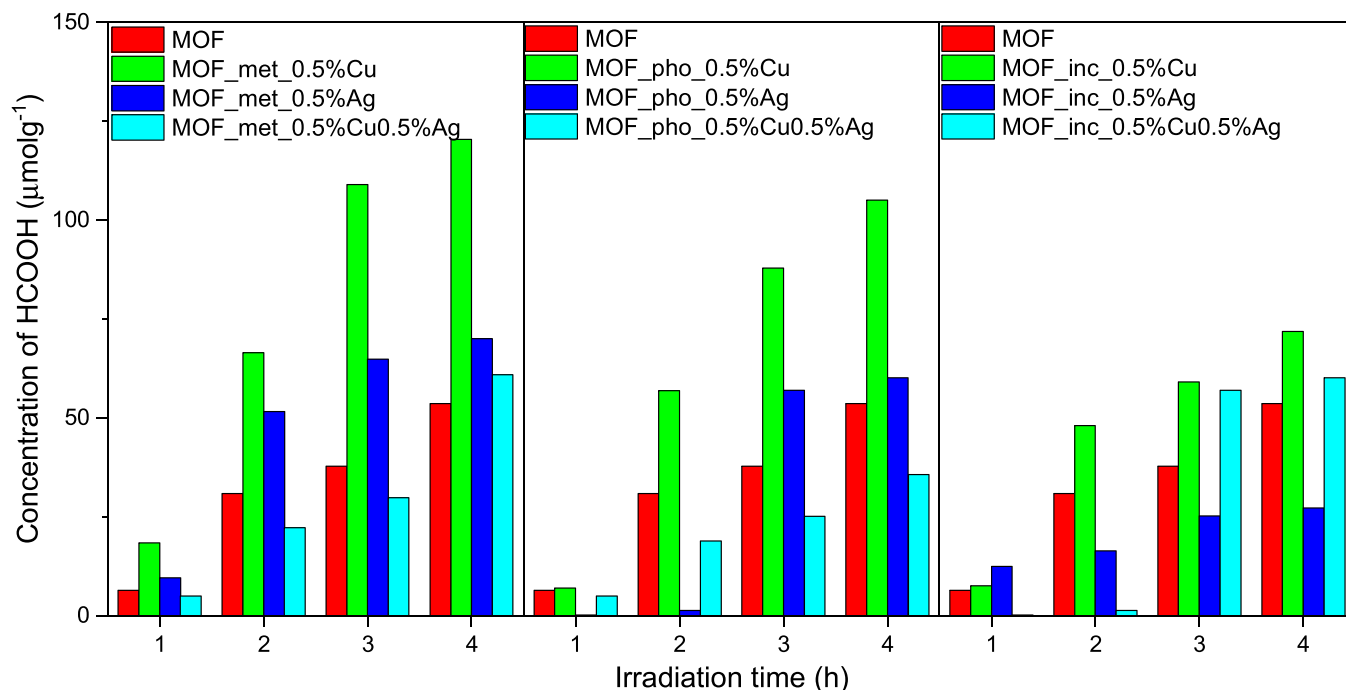
Fig. 4. HCOOH generation by the photoconversion of CO_2 under Vis-light irradiation ($\lambda > 420$ nm) using MOFs modified with Cu, Ag, and both metals via a) metalation, b) photodeposition, and c) incorporation.
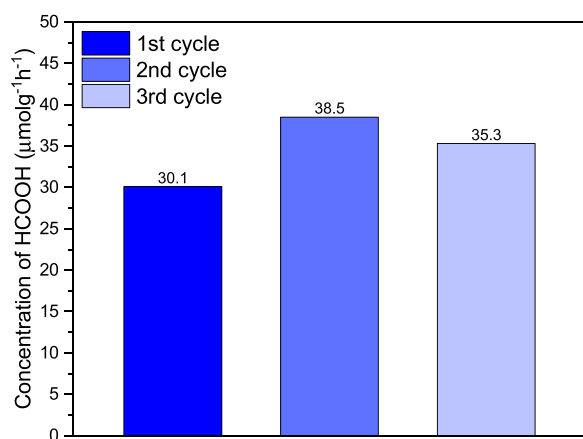

Fig. 5. Efficiency of HCOOH generation over MOF_met_0.5%_Cu during three cycles of CO_2 photoconversion to HCOOH under Vis-light irradiation ($\lambda > 420$ nm).

demonstrates the highest HCOOH production efficiency. Substantially lower heats of adsorption are observed for MOF, MOF_met_0.25%Cu, and MOF_met_1.0%Cu (14.6, 15.2, and 16.6 kJ mol^{-1}, respectively), leading to lower CO_2 photoconversion efficiencies. Generally, a positive heat of adsorption indicates that the CO_2 molecules adsorbed on the MOF surface release heat. The stronger the bond between CO_2 and MOF, the more the energy released and the more the energy needed to desorb CO_2 from the MOF surface [55]. Therefore, the stronger the bonding of CO_2 to the MOF surface, the easier the conversion of CO_2 to HCOOH.

Additionally, some studies [56,57] have revealed that the efficiency of CO_2 photoreduction to hydrocarbons strictly depends on CO_2 sorption by the photocatalyst, which is the primary component responsible for sorption [57]. In this study, no correlation was noticed between the CO_2 photoreduction efficiency and CO_2 sorption capacity. Pristine MOF exhibits a CO_2 sorption capacity of 6.16 mmol g^{-1}, which decreases to 4.15 mmol g^{-1} for the most photoactive sample MOF_met_0.5%Cu. The

lack of correlation between the CO_2 sorption capacity and photoconversion efficiency of MOF stems from the fact that photoconversion was conducted in an electrolyte consisting of AcN and TEOA, where TEOA demonstrates strong CO_2 sorption properties ($\sim$1.1 mol CO_2/TEOA mol^{-1}) [58]. Thus, TEOA can substantially increase the CO_2 sorption capacities of solutions by forming hydroxy carbonates (TEOA-HCO$_3$) [59]. Consequently, the contributions of MOF-type materials dispersed in AcN/TEOA to CO_2 sorption may be insignificant. For the tested system, MOF_met_0.5%Cu (50 mg) theoretically sorbed 0.2 mmol CO_2, whereas TEOA (2 mL) sorbed 16.7 mmol CO_2.

3.4.3. Photocatalytic stability test

Photocatalytic stability of MOF_met_0.5%Cu was investigated during 3 cycles of CO_2 photoconversion to HCOOH under Vis-light irradiation ($\lambda > 420$ nm), and the results are depicted in Fig. 5. Efficiency of CO_2 reduction to HCOOH in the first cycle is 30.1 µmol g^{-1} h^{-1} and remains at similar levels (with a slight increase) in the subsequent cycles, reaching 38.5 and 35.3 µmol g^{-1} h^{-1} in the second and third cycles, respectively. XRD patterns of pristine MOF and MOF_met_0.5%Cu before and after photocatalytic processes are shown in Fig. S16. In the XRD pattern of MOF_met_0.5%Cu, a slight decrease signal intensity at 7˚ with no change in the number or shift of reflections can be observed. Furthermore, SEM images were acquired, which confirm the unchanged structure of the material, indicating its high stability.

3.4.4. Mechanism of CO_2 photoconversion

To verify the formation of HCOOH from CO_2 via photoconversion using MOF_met_0.5%Cu, studies were performed using isotopically labeled [^{13}C] $^{13}CO_2$ instead of CO_2. Analysis of the isotopically labeled products in the obtained samples by ^{13}C NMR and ^{1}H NMR spectroscopies and headspace GC/MS confirmed the photoconversion of CO_2 to HCOOH. Photoconversion using $^{13}CO_2$ was conducted in a small reactor, in which 12.5 mg MOF_met_0.5%Cu was suspended in a 5 mL solution of TEOA (10%) in AcN-d$_6$. The resulting system was saturated with $^{13}CO_2$ and subjected to Vis-light irradiation ($\lambda > 420$ nm) for 10 h. The corresponding ^{13}C NMR spectra are shown in Fig. 6. Clear signals arising from dissolved $^{13}CO_2$ (126 ppm) and H^{13}CO$_3^-$ (159 ppm) present in the
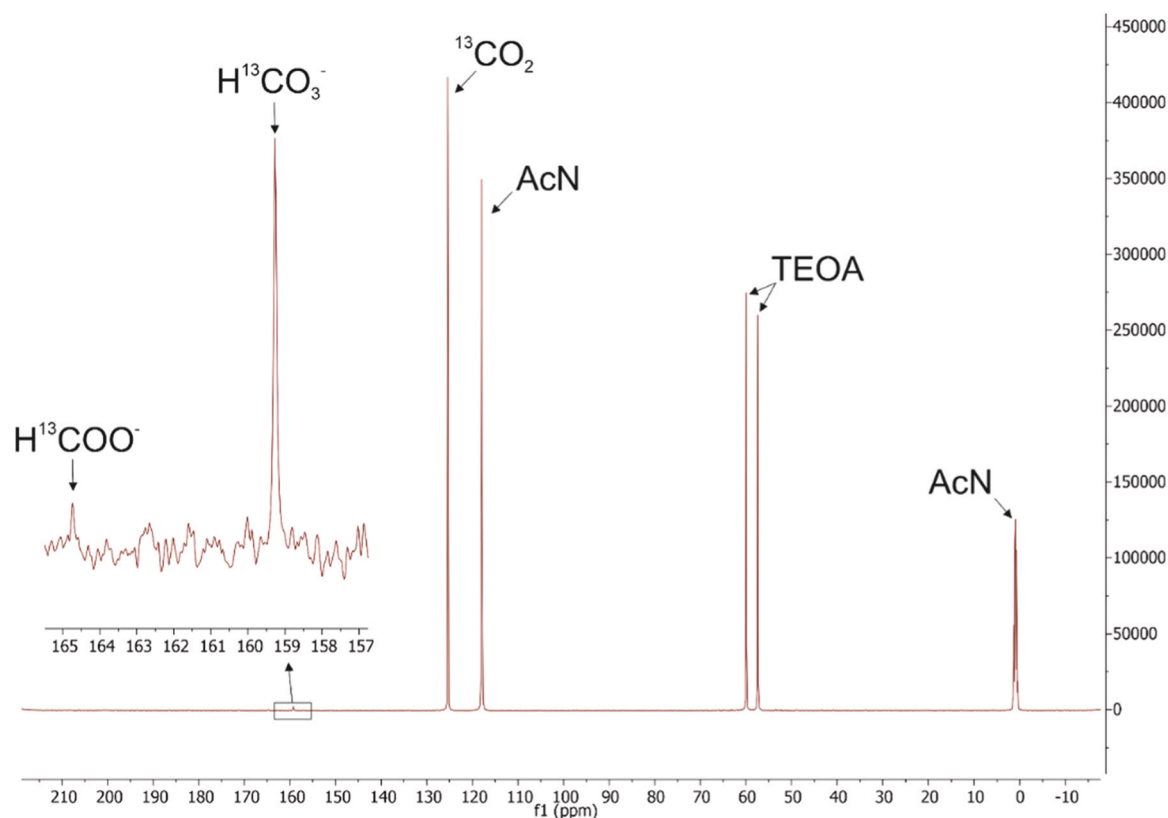
Fig. 6. ^{13}C NMR spectra of the products obtained via photoconversion using [^{13}C] CO_2 and 12.5 mg MOF_met_0.5%Cu for 10 h in 5 mL AcN/TEOA under Vis-light irradiation.

electrolyte and photoreduced H^{13}COO$^-$ (165 ppm) can be noticed [13, 60]. Note that when non-isotopic CO_2 was employed in the process, these signals were not observed. Additionally, ^{1}H NMR studies were performed on the electrolyte solution, on the HCOOH standard solution, and after 2 h of CO_2 photoconversion and photoprocessing under a N_2 atmosphere to identify protons in HCOOH. Results (Fig. S17) reveal an evident signal at 9.62 ppm corresponding to H in HCOOH formed during the photoconversion of CO_2, whereas this signal is absent in the spectrum of the sample produced via photoprocessing under a N_2 atmosphere.

The second technique employed to verify HCOOH formation from CO_2 was headspace GC/MS. Before actual GC/MS of HCOOH acquired from the sample, derivatization was conducted using ethanol [61]. During derivatization, the main reaction was the esterification of HCOOH with ethanol to form ethyl formate (Eq. 1). Moreover, because of heating and the presence of sulfuric acid as an esterification catalyst, side reactions can occur: oxidation of ethanol to acetic acid (Eq. 2), esterification of acetic acid to ethyl acetate (Eq. 3), or generation of ethyl ether (Eq. 4) [61–64].
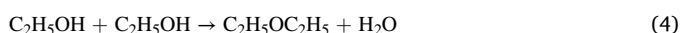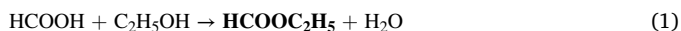
$$HCOOH + C_2H_5OH \rightarrow \textbf{HCOOC}_2\textbf{H}_5 + H_2O \tag{1}$$

$$2\ C_2H_5OH + O_2 \rightarrow 2\ CH_3COOH \tag{2}$$

$$CH_3COOH + C_2H_5OH \rightarrow CH_3COOC_2H_5 + H_2O \tag{3}$$

$$C_2H_5OH + C_2H_5OH \rightarrow C_2H_5OC_2H_5 + H_2O \tag{4}$$

Figure S18 depicts the extracted chromatograms of *m/z* 74 and 75 corresponding to the molar masses of ethyl formate and ethyl ^{13}C-formate, respectively [61,65]. Strong signals of *m/z* 74 can be noticed for the standard HCOOH solution (Fig. S18b) and CO_2 photoconversion products (Fig. S18c); in contrast, an intense signal of *m/z* 75 can be observed for the products generated via $^{13}CO_2$ photoconversion

(Fig. S18d), whereas no signals of *m/z* 74 and 75 are detected for the pure electrolyte (AcN/TEOA) (Fig. S18a). Mass spectra of the HCOOH standard solution and products acquired from the photoconversion of CO_2 and $^{13}CO_2$ are shown in Fig. S19 [65]. These spectra clearly confirm that HCOOH is produced by the photoreduction of CO_2.

Figures S18c and d depict additional signals arising from ethyl acetate and ethyl ethanoate, which may have originated from the side reactions of ethanol (Eqs. 2–4).

Mechanism of CO_2 photoconversion to HCOOH using MOF_met_0.5%Cu was proposed (Fig. 7a). In the first step, CO_2 is probably adsorbed by MOF and TEOA. Under Vis-light irradiation, MOF is excited and e$^-$/h$^+$ pairs are created in LUMO and HOMO, respectively. Next, CO_2 adsorbed on the pores and MOF surface are directly reduced to COO$^-$ by electrons. Simultaneously, the oxidation of TEOA by h$^+$ affords acetaldehyde and H$^+$ [11], and CO_2 adsorbed by TEOA is released. COO$^-$ reacts with H$^+$, forming HCO$_2^{\cdot}$, which is converted to HCOOH using e$^-$ and H$^+$ in the next step [66,67].

In addition, the presence of formic acid was confirmed after 4 h of CO_2 photoconversion using MOF_met_0.5%Cu under visible light by FTIR analysis (Figure S20). Characteristic stretching vibration bands (ν_s) of O-H bonds at 2945 and 2816 cm^{-1}, C-H at 2888 cm^{-1}, C=O at 1657 cm^{-1}, C-O at 1146 cm^{-1}, and bending vibration band (ν_b) of O-H bonds at 887 cm^{-1} and O-C-O at 563 cm^{-1}, characteristic of HCOOH, can be observed [68]

Proposed excitation mechanisms of MOF, MOF_met_0.5%Cu, MOF_inc_0.5%Cu, and MOF_pho_0.5%Cu are shown in Fig. 7b. HOMO potentials and energy gaps for pristine MOF, MOF_met_0.5%Cu, and MOF_inc_0.5%Cu were calculated from the XPS results and the Kubelka-Munk transformation of the DRS plot, respectively. Due to the composite nature of MOF_pho_0.5%Cu (MOF with Cu$_2$O), the energy gap for the MOF part was acquired from pristine MOF, whereas that for Cu$_2$O was obtained from literature data [69]. HOMO potentials for MOF and MOF_inc_0.5%Cu were 2.12 and 2.07 V and energy gaps 2.76 and
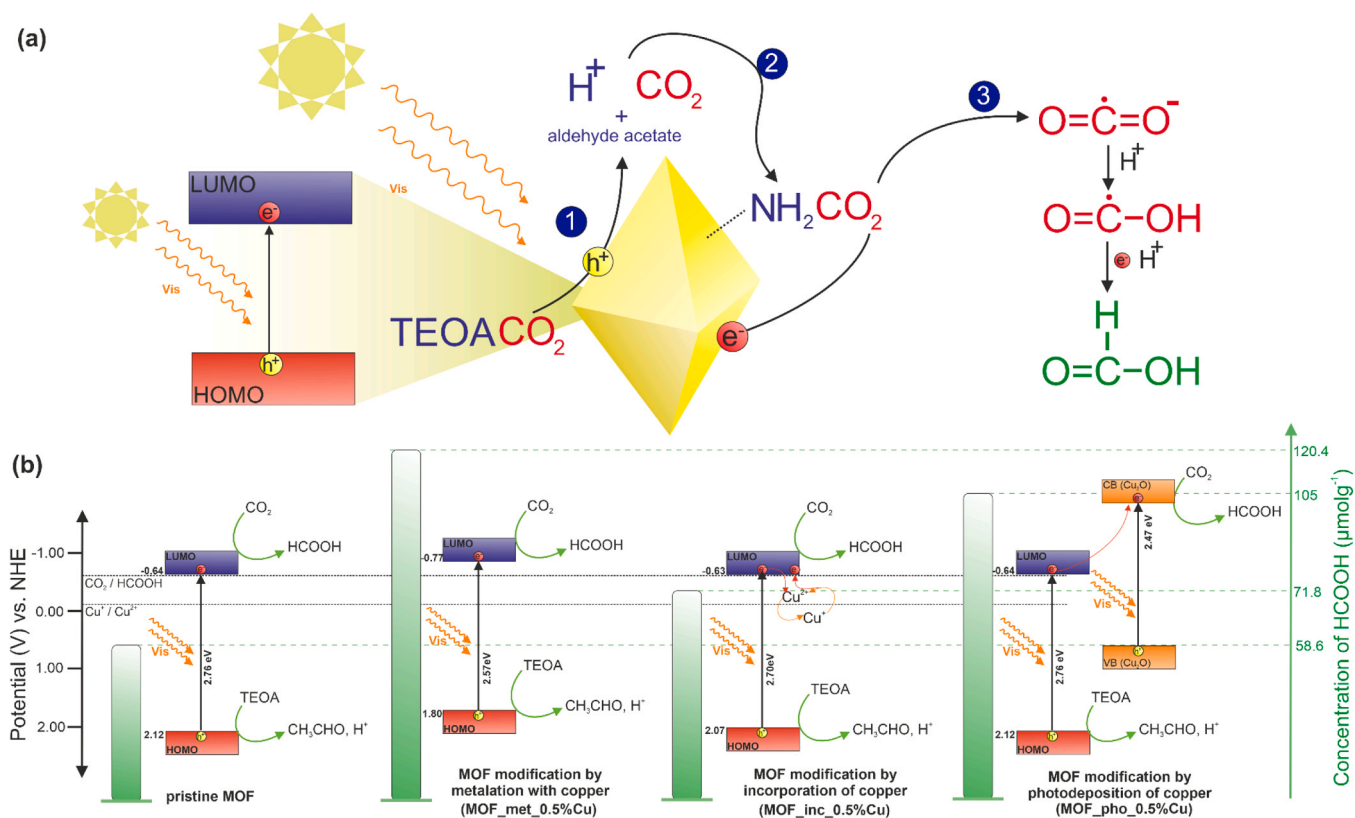
Fig. 7. (a) Proposed pathway of CO_2 photoreduction by MOF in TEOA/AcN and (b) proposed mechanism of excitation under visible-light irradiation of MOF, MOF_met_0.5%Cu, MOF_inc_0.5%Cu, and MOF_pho_0.5%Cu [26,60].

2.70 eV, respectively. This indicates that the LUMO potentials of MOF and MOF_inc_0.5%Cu reach −0.64 and −0.63 V, respectively. These values are slightly higher than the CO_2/HCOOH reduction potential (-0.61 V). The small difference between the CO_2/HCOOH reduction overpotential and LUMO band potential may have a definite impact on the low efficiency of CO_2 conversion to HCOOH (58.6 and 71.8 μmol g^{-1}) when the photocatalyst is excited with Vis-light radiation ($\lambda >$ 420 nm) [26]. Compared to MOF, MOF_inc_0.5%Cu and MOF_pho_0.5% Cu, MOF_met_0.5%Cu demonstrates the highest HCOOH generation efficiency (120.4 μmol g^{-1}) with a significantly lower energy gap of 2.57 eV and a LUMO potential of 0.77 V, effectively affecting the CO_2 photoconversion efficiency. Persistently high CO_2 photoconversion efficiency of MOF_pho_0.5%Cu (105 μmol g^{-1}) may be ascribed to the possible charge transfer from LUMO of MOF to the conduction band of Cu_2O with higher reduction potential than the LUMO potential [69].

AQE is an important parameter that describes the photoactivities of materials under irradiation with a selected wavelength range; however, information on AQEs of MOFs is lacking. AQEs of MOF_0.5%Cu in the wavelength range of 380–500 nm (action spectra analysis) are shown in Fig. 8 and Table S4. Highest AQE of 1.18% was obtained for the reaction conducted at 380 nm. AQE decreases with an increase in the applied wavelength, which appropriately corresponds with the absorption spectrum of the investigated photocatalyst MOF_met_0.5%Cu. Note that AQEs at 400, 420, and 440 nm are still similar (0.98, 0.83, and 0.75%, respectively). Comparing the acquired results with literature data is difficult because of the lack of information on these MOFs. In the case of NH_2-UiO-66 containing Ir single atoms, AQE of CO_2 reduction to HCOOH reaches 2.51% at 420 nm [70]. The yield of the as-prepared sample is also lower than that of the selected semiconductor materials, e.g., 3% for CuO-Pd/H_xMoO_{3-y} in the conversion of CO_2 to CO at 600 nm [71] and 5.23% for CoDAC-3.5 in the transformation of CO_2 to methane at 400 nm [72].
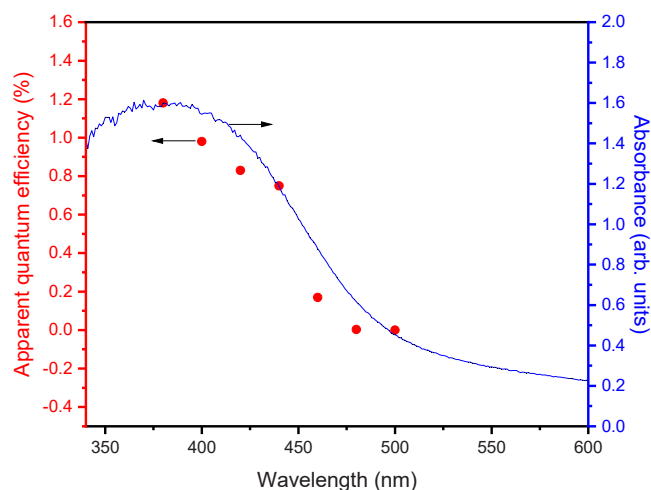

Fig. 8. AQEs for MOF_met_0.5%Cu obtained under monochromatic irradiation with wavelength in the range of 380–480 nm.

3.5. Structural similarity

In this study, the PCA approach was adopted to group the MOFs separately modified with Cu, Ag, and a combination of both metals based on their structural similarities and then to search for suggestions on possible relationships between MOF-based structures and their HCOOH production efficiencies.

For PCA, a hybrid MOF modified with Cu, Ag, or a combination of Cu and Ag was explored in the space of structural descriptors derived from experimental studies (Table 3). First two PCs (PC1 and PC2) accounted for 53.6% (27.6% from PC1 and 26.2% from PC2) of the total variance in

the dataset. As discussed in Section 2.8, a physical interpretation can be attributed to a specific PC by considering the contributions of the original descriptors to that PC, as indicated by their loading values (only the contributions of descriptors with normalized loadings higher than 0.7 are significant). We speculated that the objects, i.e., MOF modified with Cu, Ag, or a combination of Cu and Ag, located close to each other in the plot were structurally similar (Fig. 9). Thus, we distinguished three primary groups (A, B, and C) with similar structures among PC1 (Fig. 9) and three main groups (D, E, and F) among PC2 (Fig. 9). Thereafter, the structures that belonged to the six primary groups were transferred into a range scale of their photocatalytic activities, where the ranges corresponded to the standardized HCOOH generation efficiencies after 4 h ($\mu mol g^{-1}$) of photoconversion under Vis-light irradiation (Fig. S21). Thus, structurally similar MOFs exhibit the same range of activities (the same color of plot dots) that prove the correlation between the structure and HCOOH production efficiency (Fig. 9 and S21). The samples can be concluded to demonstrate different at% Ti in XPS study (XPS Ti), at%C in XPS study (XPS C) and at%O in XPS study (XPS O), and absorbances at 380 nm (Fig. 9 and S20). In addition to the loading values (Fig. S20), PC2 represents BET surface areas, pore volumes, XPS Ag, and XPS Cu of the investigated MOF structures.

Group A comprises MOF_inc_0.5%Ag, which exhibits the highest XPS O and Ti (at%) and the lowest XPS C and absorbance at 380 nm. Then, Group C that contains MOF_inc_0.5%Ag0.5%Cu demonstrates the highest absorbance at 380 nm and XPS C and the lowest XPS O and Ti (at %). In contrast, Group B consists of the rest of MOFs that exhibit similarities in the context of XPS O, XPS Ti, XPS C, and absorbance at 380 nm (at%). In the case of PC2, three groups with similar structures are observed (Fig. 9). Group D comprises MOF_met_0.5%Cu, MOF_met_0.25%Cu, MOF_met_1.0%Cu, MOF_pho_0.5%Cu, MOF_inc_0.5%Cu, and MOF_inc_0.5%Cu0.5%Ag. Group D demonstrates the lowest BET surface area ($m^2 g^{-1}$) and pore volume ($cm^3 g^{-1}$) and the highest XPS Ag (at%). Group E contains MOF_met_0.5%Cu, MOF_met_0.25%Cu, MOF_met_1.0%Cu, MOF_pho_0.5%Cu, MOF_inc_0.5%Cu, and MOF_inc_0.5% Cu0.5%Ag. Group E (Fig. 9, S20, and S21) exhibits an average BET

surface area and pore volume and higher XPS Cu (at%) than that of Group D. Nevertheless, the most active group of structures among PC2 consists of MOF_pho_0.5%Cu and MOF_met_0.5%Cu. The most active samples are represented by the highest BET surface areas and pore volumes and high XPS Cu (at%) when compared with those of Group D and E (Fig. 9, S20, and S21). Similar results are achieved via 2D HCA (Fig. S22).

4. Conclusions

In summary, herein, after examining three ways, i.e. metalation, photodeposition, and incorporation, of modifying NH$_2$-MIL-125 (Ti) with Cu and Ag, the introduction of Cu into NH$_2$-MIL-125 (Ti) by metalation is discovered to be the most beneficial for CO$_2$-to-HCOOH photoconversion; this implies that the abovementioned method is the simplest, fastest, and most effective approach for NH$_2$-MIL-125 (Ti) modification. Advanced analyses by STEM-EDS, XPS, and FTIR spectroscopy reveal that (*i*) the metal is bound to free amine groups by coordination bonds after metalation, (*ii*) the metal is incorporated into SBUs after incorporation, and (*iii*) the metal exists in the form of metal oxide NPs on the MOF surface after photodeposition.

The way of Cu introduction into MOFs affected the efficiency of CO$_2$ photoconversion into HCOOH under Vis-light irradiation (>420 nm) in the following order: metalation (30.1 $\mu mol \cdot g^{-1} \cdot h^{-1}$) > photodeposition (26.25 $\mu mol \cdot g^{-1} \cdot h^{-1}$) > incorporation into SBU (17.95 $\mu mol \cdot g^{-1} \cdot h^{-1}$). During metalation, the amount of Cu ions used for MOF modification was varied from 0.25 to 1 wt% with respect to the mass of MOF, and the optimal amount of Cu ions was discovered to be 0.5 wt%. Addition of 0.5 wt% Cu^{2+} to NH$_2$-MIL-125 (Ti) suspended in AcN resulted in MOF with 0.33 wt% Cu (MOF_met_0.5%Cu), as determined by ICP. Photoactivity of MOF_met_0.5%Cu was more than twice that of pristine MOF, and this sample maintained its efficiency and crystal structure without any visible changes during the three consecutive cycles of HCOOH generation. Furthermore, MOF_met_0.5%Cu exhibited the highest heat of CO$_2$ adsorption as compared to those of pristine MOF and MOFs
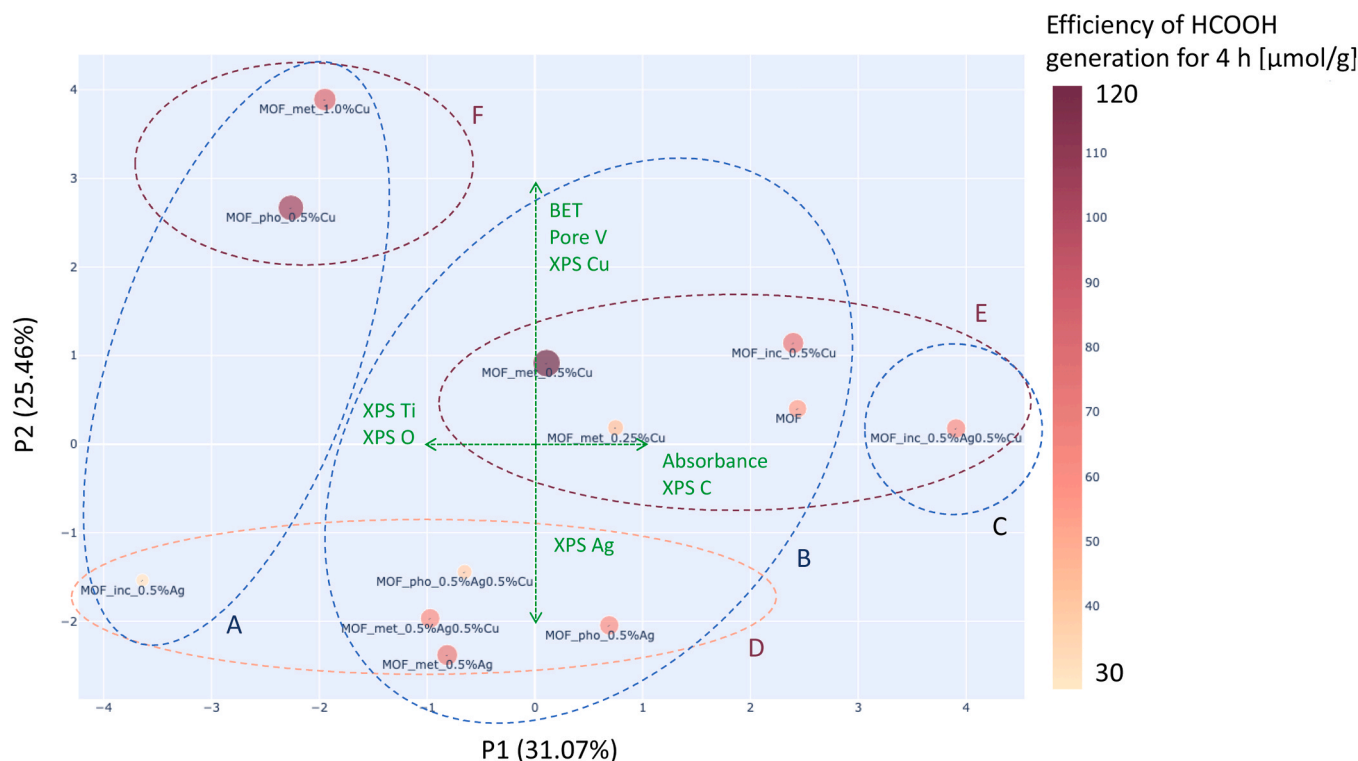

Fig. 9. Score plots obtained via the two principal component analyses performed for NH$_2$-MIL-125 (Ti)-based photocatalysts. Pink color represents the HCOOH generation efficiency under visible-light irradiation.

metalized with Cu in other amounts; this may lead to the conclusion that the stronger binding of CO_2 to the MOF surface facilitates the conversion of CO_2 to HCOOH. Existence of complexed Cu in metalized NH$_2$-MIL-125 (Ti) was confirmed by STEM-EDS, FTIR spectroscopy (956 and 1054 cm^{-1} bands attributed to the presence of Cu-N bond were detected in the FTIR spectra) and XPS (BE = 933.1 eV for Cu2p3 probably arising from the existence of metal ions coordinates).

Finally, we can conclude that the high photocatalytic activity observed for Cu-modified NH$_2$-MIL-125 can be ascribed to (i) an augmentation in the heat of CO_2 adsorption, (ii) deceleration in the recombination of excited electrons, and (iii) an increase in the over-potentials of the LUMO bands. To verify that the detected HCOOH originated from CO_2 photoconversion, $^{13}CO_2$ as a reagent, ^{13}C NMR spectroscopy, and headspace GC/MS have been employed. Experimental investigations were also supported by PCA to determine the possible relationships between the MOF-based structures and their HCOOH production efficiencies. PCA suggests that both the amount of Cu and specific surface area are key parameters in the case of modified NH$_2$-MIL-125 (Ti) employed for CO_2-to-HCOOH photoconversion, which is consistent with the results of experimental studies.

CRediT authorship contribution statement

Mateusz Adam Baluk: Writing – review & editing, Writing – original draft, Visualization, Validation, Methodology, Investigation, Formal analysis, Data curation, Conceptualization. **Aleksandra Pieczyńska**: Writing – review & editing, Methodology, Investigation. **Paweł Mazierski**: Methodology. **Malwina Kroczewska:** Investigation. **Kostiantyn Nikiforow:** Writing – original draft, Investigation. **Alicja Mikolajczyk:** Writing – original draft, Investigation, Formal analysis. **Joanna Dołżonek:** Investigation. **Justyna Łuczak:** Writing – review & editing, Resources, Project administration, Funding acquisition. **Adriana Zaleska-Medynska:** Writing – review & editing, Supervision, Resources, Project administration, Funding acquisition, Conceptualization.

Declaration of Competing Interest

The authors declare that they have no known competing financial interests or personal relationships that could have appeared to influence the work reported in this paper.

Data Availability

The data that support the findings of this study are available on request from the corresponding author (MAB and AZM)

Acknowledgments

Appendices

Supplementary information

Appendix A. Supporting information

Supplementary data associated with this article can be found in the online version at doi:10.1016/j.apcatb.2024.124107.

References

[1] E.M. Bridges, L.R. Oldeman, Global Assessment of Human-Induced Soil Degradation, ⟨Http:Dx.Doi.Org/10.1080/089030699263212⟩. 13 (2010) 319–325. https://doi.org/10.1080/089030699263212.

[2] S.P. Singh, P. Singh, Effect of CO2 concentration on algal growth: A review, Renew. Sustain. Energy Rev. 38 (2014) 172–179, https://doi.org/10.1016/J. RSER.2014.05.043.

[3] K. Li, X. An, K.H. Park, M. Khraisheh, J. Tang, A critical review of CO2 photoconversion: catalysts and reactors, Catal. Today 224 (2014) 3–12, https://doi.org/10.1016/J.CATTOD.2013.12.006.

[4] O.M. Yaghi, M.J. Kalmutzki, C.S. Diercks, Introduction to reticular chemistry: metal-organic frameworks and covalent organic frameworks, Introd. Reticular Chem. Met. Fram. Covalent Org. Fram. (2019) 1–509, https://doi.org/10.1002/9783527821099.

[5] R.A. Maia, B. Louis, W. Gao, Q. Wang, CO2 adsorption mechanisms on MOFs: a case study of open metal sites, ultra-microporosity and flexible framework, React. Chem. Eng. 6 (2021) 1118–1133, https://doi.org/10.1039/D1RE00090J.

[6] L. Pukdeejorhor, S. Wannapaiboon, J. Berger, K. Rodewald, S. Thongratkaew, S. Impeng, J. Warnan, S. Bureekaew, R.A. Fischer, Defect engineering in MIL-125-(Ti)-NH2 for enhanced photocatalytic H2 generation, J. Mater. Chem. A. 11 (2023) 9143–9151, https://doi.org/10.1039/D2TA09963B.

[7] Y. Fu, J. Wu, R. Du, K. Guo, R. Ma, F. Zhang, W. Zhu, M. Fan, Temperature modulation of defects in NH2-UiO-66(Zr) for photocatalytic CO2 reduction, RSC Adv. 9 (2019) 37733–37738, https://doi.org/10.1039/C9RA08097J.

[8] J. Yang, B. Liu, F. Ma, Study on photocatalytic degradation of CEES by ZIF-8, NTU-9 and MOF-525, IOP Conf. Ser. Earth Environ. Sci. 546 (2020) 042065, https://doi.org/10.1088/1755-1315/546/4/042065.

[9] Y. An, Y. Liu, H. Bian, Z. Wang, P. Wang, Z. Zheng, Y. Dai, M.H. Whangbo, B. Huang, Improving the photocatalytic hydrogen evolution of UiO-67 by incorporating Ce4+-coordinated bipyridinedicarboxylate ligands, Sci. Bull. 64 (2019) 1502–1509, https://doi.org/10.1016/J.SCIB.2019.07.030.

[10] Q. Li, K. Wang, H. Wang, M. Zhou, B. Zhou, Y. Li, Q. Li, Q. Wang, H.M. Shen, Y. She, Metalloporphyrin-Based Metal–Organic Frameworks for Photocatalytic Carbon Dioxide Reduction: The Influence of Metal Centers, Processes 11 (2023) 1042, https://doi.org/10.3390/PR11041042/S1.

[11] M.A. Baluk, P. Mazierski, A. Pieczyńska, K. Nikiforow, G. Trykowski, T. Klimczuk, A. Zaleska-Medynska, MOF/TiO2 erythrocyte-like heterostructures decorated by noble metals for use in hydrogen photogeneration and pollutant photodegradation, Catal. Sci. Technol. (2023), https://doi.org/10.1039/D3CY00531C.

[12] G.E.M. Schukraft, B. Moss, A.G. Kafizas, C. Petit, Effect of band bending in photoactive MOF-based heterojunctions, ACS Appl. Mater. Interfaces 14 (2022) 19342–19352, https://doi.org/10.1021/ACSAMI.2C00335/ASSET/IMAGES/LARGE/AM2C00335_0006.JPEG.

[13] Y. Fu, H. Yang, R. Du, G. Tu, C. Xu, F. Zhang, M. Fan, W. Zhu, Enhanced photocatalytic CO2 reduction over Co-doped NH2-MIL-125(Ti) under visible light, RSC Adv. 7 (2017) 42819–42825, https://doi.org/10.1039/C7RA06324E.

[14] S. Chen, G. Hai, H. Gao, X. Chen, A. Li, X. Zhang, W. Dong, Modulation of the charge transfer behavior of Ni(II)-doped NH2-MIL-125(Ti): Regulation of Ni ions content and enhanced photocatalytic CO2 reduction performance, Chem. Eng. J. 406 (2021) 126886, https://doi.org/10.1016/J.CEJ.2020.126886.

[15] Y. Zhao, W. Cai, J. Chen, Y. Miao, Y. Bu, A highly efficient composite catalyst constructed from NH2-MIL-125(Ti) and reduced graphene oxide for CO2 photoreduction, Front. Chem. 7 (2019) 789, https://doi.org/10.3389/FCHEM.2019.00789/BIBTEX.

[16] X.M. Cheng, X.Y. Dao, S.Q. Wang, J. Zhao, W.Y. Sun, Enhanced photocatalytic CO2 reduction activity over NH2-MIL-125(Ti) by facet regulation, ACS Catal. 11 (2021) 650–658, https://doi.org/10.1021/ACSCATAL.0C04426/SUPPL_FILE/CS0C04426_SI_001.PDF.

[17] M. Sun, F. Yu, J. Wang, Y. Wang, X. Jing, C. Duan, d-NH2-MIL-125 doped with Cu NPs for light-driven hydrogen evolution, Chem. Commun. 59 (2023) 8456–8459, https://doi.org/10.1039/D3CC01770B.

[18] W. Cui, J. Shang, H. Bai, J. Hu, D. Xu, J. Ding, W. Fan, W. Shi, In-situ implantation of plasmonic Ag into metal-organic frameworks for constructing efficient Ag/NH2-MIL-125/TiO2 photoanode, Chem. Eng. J. 388 (2020) 124206, https://doi.org/10.1016/J.CEJ.2020.124206.

[19] V. Muelas-Ramos, C. Belver, J.J. Rodriguez, J. Bedia, Synthesis of noble metal-decorated NH2-MIL-125 titanium MOF for the photocatalytic degradation of acetaminophen under solar irradiation, Sep. Purif. Technol. 272 (2021) 118896, https://doi.org/10.1016/J.SEPPUR.2021.118896.

[20] R. Kaur, A. Kaur, R. Kaur, S. Singh, M.S. Bhatti, A. Umar, S. Baskoutas, S.K. Kansal, Cu-BTC metal organic framework (MOF) derived Cu-doped TiO2 nanoparticles and their use as visible light active photocatalyst for the decomposition of ofloxacin (OFX) antibiotic and antibacterial activity, Adv. Powder Technol. 32 (2021) 1350–1361, https://doi.org/10.1016/J.APT.2021.02.037.

[21] K. Bhattacharyya, G.P. Mane, V. Rane, A.K. Tripathi, A.K. Tyagi, Selective CO2Photoreduction with Cu-Doped TiO2Photocatalyst: Delineating the Crucial Role of Cu-Oxidation State and Oxygen Vacancies, J. Phys. Chem. C. (2021), https://doi.org/10.1021/ACS.JPCC.0C08441/SUPPL_FILE/JP0C08441_SI_001.PDF.

[22] Y. Hori, K. Kikuchi, S. Suzuki, Production of CO and CH4 in electrochemical reduction of CO2 at metal electrodes in aqueous hydrogencarbonate solution, Chem. Lett. 14 (1985) 1695–1698, https://doi.org/10.1246/CL.1985.1695.

[23] Y. Hori, A. Murata, R. Takahashi, Formation of hydrocarbons in the electrochemical reduction of carbon dioxide at a copper electrode in aqueous solution, J. Chem. Soc. Faraday Trans. 1 Phys. Chem. Condens. Phases. 85 (1989) 2309–2326, https://doi.org/10.1039/F19898502309.

[24] Y. Hori, H. Wakebe, T. Tsukamoto, O. Koga, Electrocatalytic process of CO selectivity in electrochemical reduction of CO2 at metal electrodes in aqueous media, Electrochim. Acta 39 (1994) 1833–1839, https://doi.org/10.1016/0013-4686(94)85172-7.

[25] S. Xu, E.A. Carter, Theoretical Insights into Heterogeneous (Photo)electrochemical CO2 Reduction, Chem. Rev. 119 (2019) 6631–6669, https://doi.org/10.1021/ACS.CHEMREV.8B00481.

[26] D. Ao, J. Zhang, H. Liu, Visible-light-driven photocatalytic degradation of pollutants over Cu-doped NH2-MIL-125(Ti), J. Photochem. Photobiol. A Chem. 364 (2018) 524–533, https://doi.org/10.1016/J.JPHOTOCHEM.2018.06.044.

[27] S. Hu, M. Liu, K. Li, Y. Zuo, A. Zhang, C. Song, G. Zhang, X. Guo, Solvothermal synthesis of NH2-MIL-125(Ti) from circular plate to octahedron, CrystEngComm 16 (2014) 9645–9650, https://doi.org/10.1039/C4CE01545B.

[28] J. Strunk, Separating fiction from fact for photocatalytic CO2 reduction, 2023, Nat. Chem. 159 (15) (2023) 1209–1211, https://doi.org/10.1038/s41557-023-01293-z.

[29] O. Cavdar, A. Malankowska, D. Amgar, P. Mazierski, J. Łuczak, W. Lisowski, A. Zaleska-Medynska, Remarkable visible-light induced hydrogen generation with ZnIn2S4 microspheres/CuInS2 quantum dots photocatalytic system, Int. J. Hydrog. Energy 46 (2021) 486–498, https://doi.org/10.1016/J.IJHYDENE.2020.09.212.

[30] M. Miodyńska, A. Mikolajczyk, P. Mazierski, T. Klimczuk, W. Lisowski, G. Trykowski, A. Zaleska-Medynska, Lead-free bismuth-based perovskites coupled with g-C3N4: A machine learning based novel approach for visible light induced degradation of pollutants, Appl. Surf. Sci. 588 (2022) 152921, https://doi.org/10.1016/J.APSUSC.2022.152921.

[31] S. Liu, Q. Zou, Y. Ma, W. Sun, Y. Li, J. Zhang, C. Zhang, L. He, Y. Sun, Q. Chen, B. Liu, H. Zhang, K. Zhang, A novel amorphous CoSx/NH2-MIL-125 composite for photocatalytic degradation of rhodamine B under visible light, J. Mater. Sci. 55 (2020) 16171–16183, https://doi.org/10.1007/S10853-020-05210-4/FIGURES/9.

[32] A.H. Sabzevar, G.R. Hashemitabar, M. Rad, J. Vatandoost, Synthesis and Biological Properties of Silver Chloride Nanoparticles Using Cell-free Extracts of Aeromonas hydrophila and Antibacterial Activity against Drug-Resistant Bacteria, Braz. Arch. Biol. Technol. 64 (2021) e21210010, https://doi.org/10.1590/1678-4324-2021210010.

[33] A. Ahmad, J. Liu, X. Liu, L. Li, Y. Xu, X. Guo, Synthesis of Ag2O nano-catalyst in the spherical polyelectrolyte brushes and its application in visible photo driven degradation of dye, E-Polym. 16 (2016) 57–63, https://doi.org/10.1515/EPOLY-2015-0194/MACHINEREADABLECITATION/RIS.

[34] J. Du, Y. Zhao, J. Chen, P. Zhang, L. Gao, M. Wang, C. Cao, W. Wen, C. Zhu, Difunctional Cu-doped carbon dots: catalytic activity and fluorescence indication for the reduction reaction of p-nitrophenol, RSC Adv. 7 (2017) 33929–33936, https://doi.org/10.1039/C7RA05383E.

[35] E. Daublytė, A. Zdaniauskienė, T. Charkova, Microwave synthesis of silver core-silica decorated nanoparticles, Chemija 33 (2022). ⟨http://opensubmissionsystem.com/index.php/chemija/article/view/7⟩ (accessed August 18, 2023).

[36] G. Agostini, C. Lamberti, Characterization of Semiconductor Heterostructures and Nanostructures, Charact. Semicond. Heterostruct. Nanostruct. (2008), https://doi.org/10.1016/B978-0-444-53099-8.X0001-2.

[37] J. Wang, A.S. Cherevan, C. Hannecart, S. Naghdi, S.P. Nandan, T. Gupta, D. Eder, Ti-based MOFs: New insights on the impact of ligand composition and hole scavengers on stability, charge separation and photocatalytic hydrogen evolution, Appl. Catal. B Environ. 283 (2021) 119626, https://doi.org/10.1016/J.APCATB.2020.119626.

[38] M. Kozak, P. Mazierski, M. Baluk, J. Żebrowska, W. Lisowski, G. Trykowski, P. Skowron, A. Zaleska-Medynska, Anodized multi – component titanium alloys carrying antibacterial features, Appl. Surf. Sci. 613 (2023) 156009, https://doi.org/10.1016/J.APSUSC.2022.156009.

[39] S.R. Eun, S. Mavengere, J.S. Kim, Preparation of Ag-TiO2/Sr4Al14O25:Eu2+,Dy3+ photocatalyst on phosphor beads and its photoreaction characteristics, Page 261, Catal 2021 Vol. 11 (11) (2021) 261, https://doi.org/10.3390/CATAL11110261.

[40] J. Moulder, W. Stickle, P. Sobol, K. Bomben, Handbook of Standard Spectra for Identification and Interpretation of XPS Data, Perkin-Elmer Corp. (1992) 260. ⟨https://search.worldcat.org/title/27133797⟩ (accessed January 16, 2024).

[41] F.L. Liu, Z.H. Xu, X.Y. Zhang, X.P. Wang, D. Sun, Unusual N?H activation of 2-aminopyrimidine: supramolecular assembly into an agi metal–organic framework, Chem. – Asian J. 9 (2014) 452–456, https://doi.org/10.1002/ASIA.201301244.

[42] B. Mortada, T.A. Matar, A. Sakaya, H. Atallah, Z. Kara Ali, P. Karam, M. Hmadeh, Postmetalated zirconium metal organic frameworks as a highly potent bactericide, Inorg. Chem. 56 (2017) 4739–4744, https://doi.org/10.1021/ACS.INORGCHEM.7B00429/SUPPL_FILE/IC7B00429_SI_001.PDF.

[43] M.C. Biesinger, Advanced analysis of copper X-ray photoelectron spectra, Surf. Interface Anal. 49 (2017) 1325–1334, https://doi.org/10.1002/SIA.6239.

[44] P.A. Bharad, A.V. Nikam, F. Thomas, C.S. Gopinath, CuOx-TiO2 Composites: electronically integrated nanocomposites for solar hydrogen generation, ChemistrySelect 3 (2018) 12022–12030, https://doi.org/10.1002/SLCT.201802047.

[45] L. Li, X. Chen, X. Quan, F. Qiu, X. Zhang, Synthesis of CuO x/TiO2Photocatalysts with Enhanced Photocatalytic Performance, ACS Omega (2022), https://doi.org/10.1021/ACSOMEGA.2C07364/ASSET/IMAGES/LARGE/AO2C07364_0010.JPEG.

[46] F. Zhang, Y.H. Li, M.Y. Qi, Z.R. Tang, Y.J. Xu, Boosting the activity and stability of Ag-Cu2O/ZnO nanorods for photocatalytic CO2 reduction, Appl. Catal. B Environ. 268 (2020) 118380, https://doi.org/10.1016/J.APCATB.2019.118380.

[47] J. Jin, Porphyrin-based metal–organic framework catalysts for photoreduction of CO2: understanding the effect of node connectivity and linker metalation on activity, N. J. Chem. 44 (2020) 15362–15368, https://doi.org/10.1039/D0NJ03507F.

[48] D. Sun, Y. Fu, W. Liu, L. Ye, D. Wang, L. Yang, X. Fu, Z. Li, Studies on photocatalytic CO2 reduction over NH2-Uio-66(Zr) and its derivatives: towards a better understanding of photocatalysis on metal–organic frameworks, Chem. – A Eur. J. 19 (2013) 14279–14285, https://doi.org/10.1002/CHEM.201301728.

[49] M. Perfecto-Irigaray, I. Merino-Garcia, J. Albo, G. Beobide, O. Castillo, A. Luque, S. Pérez-Yáñez, Copper(II)-porphyrin functionalized titanium(IV) metal-organic aerogels for the visible-light driven conversion of CO2 to alcohols, Mater. Today Energy 36 (2023) 101346, https://doi.org/10.1016/J.MTENER.2023.101346.

[50] A. Angulo-Ibáñez, M. Perfecto-Irigaray, I. Merino-Garcia, N. Luengo, A. M. Goitandia, J. Albo, E. Aranzabe, G. Beobide, O. Castillo, S. Pérez-Yáñez, Metal-organic aerogels based on titanium(IV) for visible-light conducted CO2 photoreduction to alcohols, Mater. Today Energy 30 (2022) 101178, https://doi.org/10.1016/J.MTENER.2022.101178.

[51] N. Landaluce, M. Perfecto-Irigaray, J. Albo, G. Beobide, O. Castillo, A. Irabien, A. Luque, A.S.J. Méndez, A.E. Platero-Prats, S. Pérez-Yáñez, Copper(II) invigorated EHU-30 for continuous electroreduction of CO2 into value-added chemicals, Sci. Rep. 2022 121. 12 (1) (2022) 7, https://doi.org/10.1038/s41598-022-11846-w.

[52] M. Perfecto-Irigaray, J. Albo, G. Beobide, O. Castillo, A. Irabien, S. Pérez-Yáñez, Synthesis of heterometallic metal–organic frameworks and their performance as electrocatalyst for CO2 reduction, RSC Adv. 8 (2018) 21092–21099, https://doi.org/10.1039/C8RA02676A.

[53] J. Albo, M. Perfecto-Irigaray, G. Beobide, A. Irabien, Cu/Bi metal-organic framework-based systems for an enhanced electrochemical transformation of CO2 to alcohols, J. CO2 Util. 33 (2019) 157–165, https://doi.org/10.1016/J.JCOU.2019.05.025.

[54] J. Albo, D. Vallejo, G. Beobide, O. Castillo, P. Castaño, A. Irabien, Copper-based metal–organic porous materials for CO2 electrocatalytic reduction to alcohols, ChemSusChem 10 (2017) 1100–1109, https://doi.org/10.1002/CSSC.201600693.

[55] W.A. Brown, R. Kose, D.A. King, The role of adsorption heats and bond energies in the assignment of surface reaction products: ethyne and ethene on Ni{110}, J. Mol. Catal. A Chem. 141 (1999) 21–29, https://doi.org/10.1016/S1381-1169(98)00246-5.

[56] M. Flores-Flores, E. Luévano-Hipólito, L.M. Torres-Martínez, T.O. Do, CO2 adsorption and photocatalytic reduction over Mg(OH)2/CuO/Cu2O under UV-Visible light to solar fuels, Mater. Chem. Phys. 227 (2019) 90–97, https://doi.org/10.1016/J.MATCHEMPHYS.2019.01.062.

[57] M.A. Ávila-López, E. Luévano-Hipólito, L.M. Torres-Martínez, CO2 adsorption and its visible-light-driven reduction using CuO synthesized by an eco-friendly sonochemical method, J. Photochem. Photobiol. A Chem. 382 (2019) 111933, https://doi.org/10.1016/J.JPHOTOCHEM.2019.111933.

[58] A. Chakma, J.P. Lemonier, E. Chornet, R.P. Overend, Absorption of CO2 by aqueous triethanolamine (TEA) solutions in a high shear jet absorber, Gas. Sep. Purif. 3 (1989) 65–70, https://doi.org/10.1016/0950-4214(89)85003-0.

[59] D. Ohde, B. Thomas, S. Matthes, Z. Percin, C. Engelmann, P. Bubenheim, K. Terasaka, M. Schlüter, A. Liese, Fine Bubble-based CO2 Capture Mediated by Triethanolamine Coupled to Whole Cell Biotransformation, Chem. Ing. Tech. 91 (2019) 1822–1826, https://doi.org/10.1002/CITE.201900113.

[60] Y. Fu, D. Sun, Y. Chen, R. Huang, Z. Ding, X. Fu, Z. Li, An amine-functionalized titanium metal–organic framework photocatalyst with visible-light-induced activity for CO2 reduction, Angew. Chem. Int. Ed. 51 (2012) 3364–3367, https://doi.org/10.1002/ANIE.201108357.

[61] D. Zhou, Q. Hou, W. Liu, X. Ren, Rapid determination of formic and acetic acids in biomass hydrolysate by headspace gas chromatography, J. Ind. Eng. Chem. 47 (2017) 281–287, https://doi.org/10.1016/J.JIEC.2016.11.044.

[62] S. Mostrou, A. Nagl, M. Ranocchiari, K. Föttinger, J.A. Van Bokhoven, The catalytic and radical mechanism for ethanol oxidation to acetic acid, Chem. Commun. 55 (2019) 11833–11836, https://doi.org/10.1039/C9CC05813C.

[63] N. Calvar, B. González, A. Dominguez, Esterification of acetic acid with ethanol: reaction kinetics and operation in a packed bed reactive distillation column, Chem. Eng. Process. Process. Intensif. 46 (2007) 1317–1323, https://doi.org/10.1016/J.CEP.2006.10.007.

[64] S.W. Colley, J. Tabatabaei, K.C. Waugh, M.A. Wood, The detailed kinetics and mechanism of ethyl ethanoate synthesis over a Cu/Cr2O3 catalyst, J. Catal. 236 (2005) 21–33, https://doi.org/10.1016/J.JCAT.2005.09.012.

[65] D.Van Raalte, A.G. Harrison, IONIZATION AND DISSOCIATION OF FORMATE ESTERS BY ELECTRON IMPACT, ⟨Https.Doi.Org/10.1139/V63-296⟩. 41 (2011) 2054–2059. https://doi.org/10.1139/V63-296.

[66] S. Matsuoka, T. Kohzuki, C. Pac, A. Ishida, S. Takamuku, M. Kusaba, N. Nakashima, S. Yanagida, Photocatalysis of oligo(p-phenylenes). Photochemical reduction of carbon dioxide with triethylamine, J. Phys. Chem. 96 (1992) 4437–4442, https://doi.org/10.1021/J100190A057/ASSET/J100190A057.FP.PNG_V03.

[67] T.N. Gemeda, L.H. Chang, Y.T. Liang, V.H.K. Phan, G. Fadhilah, F. Prasetyo, M. T. Ahmed, A Recent Review on Photocatalytic CO2 Reduction in Generating Sustainable Carbon-Based Fuels, Green. Energy Technol. (2023) 205–261, https://doi.org/10.1007/978-981-19-6748-1_4/COVER.

[68] A. Bergantini, S. Pilling, H. Rothard, P. Boduch, D.P.P. Andrade, Processing of formic acid-containing ice by heavy and energetic cosmic ray analogues, Mon. Not. R. Astron. Soc. 437 (2014) 2720–2727, https://doi.org/10.1093/MNRAS/STT2082.

[69] Y. Yang, D. Xu, Q. Wu, P. Diao, Cu2O/CuO bilayered composite as a high-efficiency photocathode for photoelectrochemical hydrogen evolution reaction, Sci. Rep. 2016 61. 6 (2016) 1–13, https://doi.org/10.1038/srep35158.

[70] Y.C. Hao, L.W. Chen, J. Li, Y. Guo, X. Su, M. Shu, Q. Zhang, W.Y. Gao, S. Li, Z.L. Yu, L. Gu, X. Feng, A.X. Yin, R. Si, Y.W. Zhang, B. Wang, C.H. Yan, Metal-organic framework membranes with single-atomic centers for photocatalytic CO2 and O2

reduction, 2021 121, Nat. Commun. 12 (2021) 1–11, https://doi.org/10.1038/s41467-021-22991-7.

[71] H. Yin, J. Li, New insight into photocatalytic CO2 conversion with nearly 100% CO selectivity by CuO-Pd/HxMoO3−y hybrids, Appl. Catal. B Environ. 320 (2023) 121927, https://doi.org/10.1016/J.APCATB.2022.121927.

[72] J. Wang, E. Kim, D.P. Kumar, A.P. Rangappa, Y. Kim, Y. Zhang, T.K. Kim, Highly durable and fully dispersed cobalt diatomic site catalysts for CO2 photoreduction to CH4, Angew. Chem. 134 (2022) e202113044, https://doi.org/10.1002/ANGE.202113044.